

CONTROLLING STIMULATED BRILLOUIN/RAMAN SCATTERING IN HIGH POWER FIBER LASERS

**Cody Mart
Ben Pulford
Khanh Kieu**

**University of Arizona
888 N Euclid Ave
Tucson, AZ 85719-4824**

9 August 2017

Final Report

APPROVED FOR PUBLIC RELEASE. DISTRIBUTION IS UNLIMITED



**AIR FORCE RESEARCH LABORATORY
Directed Energy Directorate
3550 Aberdeen Ave SE
AIR FORCE MATERIEL COMMAND
KIRTLAND AIR FORCE BASE, NM 87117-5776**

NOTICE AND SIGNATURE PAGE

Using Government drawings, specifications, or other data included in this document for any purpose other than Government procurement does not in any way obligate the U.S. Government. The fact that the Government formulated or supplied the drawings, specifications, or other data does not license the holder or any other person or corporation; or convey any rights or permission to manufacture, use, or sell any patented invention that may relate to them.

Qualified requestors may obtain copies of this report from the Defense Technical Information Center (DTIC) (<http://www.dtic.mil>).

AFRL-RD-PS-TR-2017-0043 HAS BEEN REVIEWED AND IS APPROVED FOR PUBLICATION IN ACCORDANCE WITH ASSIGNED DISTRIBUTION STATEMENT.

PULFORD.BENJAMI
N.NOAH.1299674262

Digitally signed by
PULFORD.BENJAMIN.NOAH.129
9674262
Date: 2017.12.14 13:25:59 -07'00'

BENJAMIN PULFORD, DR-II, DAF
Work Unit Manager

WOOD.KENTON.T
.1151077656

Digitally signed by
WOOD.KENTON.T.1151077656
Date: 2018.01.12 14:49:55 -07'00'

KENTON T. WOOD, DR-IV, DAF
Chief, Laser Division

This report is published in the interest of scientific and technical information exchange, and its publication does not constitute the Government's approval or disapproval of its ideas or findings.

REPORT DOCUMENTATION PAGE				Form Approved OMB No. 0704-0188	
Public reporting burden for this collection of information is estimated to average 1 hour per response, including the time for reviewing instructions, searching existing data sources, gathering and maintaining the data needed, and completing and reviewing this collection of information. Send comments regarding this burden estimate or any other aspect of this collection of information, including suggestions for reducing this burden to Department of Defense, Washington Headquarters Services, Directorate for Information Operations and Reports (0704-0188), 1215 Jefferson Davis Highway, Suite 1204, Arlington, VA 22202-4302. Respondents should be aware that notwithstanding any other provision of law, no person shall be subject to any penalty for failing to comply with a collection of information if it does not display a currently valid OMB control number. PLEASE DO NOT RETURN YOUR FORM TO THE ABOVE ADDRESS.					
1. REPORT DATE 08-08-2017		2. REPORT TYPE Final Report		3. DATES COVERED (From - To) 8 July 2015- 8 August 2017	
4. TITLE AND SUBTITLE Controlling Stimulated Brillouin/Raman Scattering in High Power Fiber Lasers				5a. CONTRACT NUMBER FA9451-15-1-0042	
				5c. PROGRAM ELEMENT NUMBER	
6. AUTHOR(S) Cody Mart, Ben Pulford, Khanh Kieu				5d. PROJECT NUMBER	
				5e. TASK NUMBER	
				5f. WORK UNIT NUMBER D08H	
7. PERFORMING ORGANIZATION NAME(S) AND ADDRESS(ES) University of Arizona 888 N. Euclid Ave Tucson, AZ 85721				8. PERFORMING ORGANIZATION REPORT NUMBER	
9. SPONSORING / MONITORING AGENCY NAME(S) AND ADDRESS(ES) Air Force Research Laboratory 3550 Aberdeen Ave SE Kirtland AFB. NM 87117-5776				10. SPONSOR/MONITOR'S ACRONYM(S) AFRL/RDLT	
				11. SPONSOR/MONITOR'S REPORT NUMBER(S) AFRL-RD-PS-TR-2017-0043	
12. DISTRIBUTION / AVAILABILITY STATEMENT Approved for public release. Distribution is unlimited.					
13. SUPPLEMENTARY NOTES Government Purpose Rights					
14. ABSTRACT This research addressed suppression of stimulated Brillouin/Raman scattering in high power fiber lasers. The work was done by Mr. Cody Mart under this research grant. Dr. Ben Pulford provided expert mentorship and laboratory space at the Air Force Research Lab (AFRL) New Mexico. Mr. Mart successfully defended his dissertation using the results reported herein in summer 2017. Detailed discussion of research activities and outcomes are described in this final report. More information on the research work and background information can be also found in Mr. Mart's dissertation.					
15. SUBJECT TERMS Fiber Amplifier, Microstructured Fiber, Stimulated Raman Scattering, Stimulated Brillouin Scattering					
16. SECURITY CLASSIFICATION OF:			17. LIMITATION OF ABSTRACT SAR	18. NUMBER OF PAGES 74	19a. NAME OF RESPONSIBLE PERSON Benjamin Pulford
a. REPORT Unclassified	b. ABSTRACT Unclassified	c. THIS PAGE Unclassified			19b. TELEPHONE NUMBER (include area code) 505-846-3451

Table of Contents

1. Summary	1
2. Introduction	1
3. Methods, Assumptions, and Procedures	3
4. Results and Discussion	5
4.1 Experimental and Theoretical Investigations of Stimulated Brillouin Scattering	5
4.1.1 SBS theory	5
4.1.2 Pump Probe Theory	10
4.1.3 Comparison of Dual Source and Phase Modulator Systems: Phase Modulator System and Results	15
4.1.4 Comparison of Dual Source and Phase Modulator Systems: Dual Source System and Results	18
4.1.5 Brillouin Gain Spectroscopy of All-Solid Ytterbium-doped Photonic Bandgap Fiber	22
4.1.6 Brillouin Gain Spectroscopy of Hybrid Microstructured Fiber	26
4.1.7 Theoretical Examination of SBS in Microstructured Fibers	29
4.2 Power Scaling Microstructured Fiber Amplifiers	35
4.2.1. MI Theory	35
4.2.2 Counter-pumped Amplifier	41
4.2.3 Hybrid Microstructured Fiber Power Scaling	43
4.2.4 All-Solid Photonic Bandgap Fiber Power Scaling	54
4.2.5 Comparison and Discussion	57
5. Conclusion	59
6. Reference	61
List of Acronyms	65

List of figures

Figure 1: The two interacting optical fields and the acoustic wave are shown schematically along with direction of propagation. The laser field polarized in the x-direction, $E_{x,\text{laser}}$ scatters to form the optical Stokes field, $E_{x,\text{Stokes}}$, and an acoustic displacement, a_{ac}	6
Figure 2: Fiber amplifier schematics for co-pumped, counter-pumped, and two-tone configurations are shown. In the two-tone schematic, a wavelength division multiplexer is a photonic component that couples two fibers of differing wavelengths in the same fiber core. A tapered fiber bundle evanescently couples multimode fibers into the cladding mode of a double-clad fiber.....	8
Figure 3: The evolution of the laser signal along the length of the fiber in a co-pumped (red) and counter-pumped (blue) amplifier configuration are shown above.....	9
Figure 4: The evolution of the laser signal along the length of the fiber with a single laser at 1064 nm (red) is shown with a two-tone amplifier with an intermediate laser at 1040 nm (green) and signal laser at 1064 nm.....	10
Figure 5: Pump and Probe power coupling schematics for the dual-source (left) and phase modulated (right) BGS methods are shown.....	12
Figure 6: Simulated BGS for amplified probe and depleted pump are shown along with locations of the boundary conditions used for numerical simulations.....	15
Figure 7: A pump probe design schematic for the phase modulator system is shown..	17
Figure 8: Brillouin Gain Spectra for the OFS fiber using the phase modulator method along with the estimated g_B at a range of pump powers tested.....	18
Figure 9: A pump probe design schematic for the dual source system is shown.....	19
Figure 10: Brillouin Gain Spectra for the OFS fiber using the dual-source method is shown along with the g_B estimated vs pump power.....	20
Figure 11: Brillouin Gain Spectra for the OFS fiber using the dual-source and phase modulator methods are shown above. Each is pumped with the same power.....	21
Figure 12: The experimental BGS, scaled to the estimated g_B is shown above.....	24
Figure 13: The g_B that best matched simulated and experimental data at each pump power tested is shown above for the PBGF. This data was subsequently scaled to account for effects of a non-PM fiber.....	25

Figure 14: The experimental BGS, scaled to the estimated g_B is shown above for the hybrid fiber. Also shown is a long-range scan revealing a peak due to the pure-silica annulus (top).....	28
Figure 15: The g_B that best matched simulated and experimental data at each pump power tested is shown above for the hybrid fiber.....	29
Figure 16: CAD designs for the core of the PBGF. The left design was with coarse core sub-segmentation and the right employs core sub-segmentation with Yb-active regions that are 850 nm in diameter within a hexagonal shell.....	33
Figure 17: Simulated BG spectra of the coarsely segmented (left) and finely segmented PBGF models are shown above.....	33
Figure 18: Simulated acoustic displacements showing the acoustic energy density at each Brillouin frequency response is shown above. Responses at 16.3 GHz are pure silica and responses at 15.45 GHz are Yb-active regions.....	34
Figure 19: Longitudinal optical interference pattern in LMA PCF whose origin is conjectured as modal interference shown as bright and dark sites for Yb-photoluminescence. The rod is 15 cm long with a 100 μ m core diameter.....	36
Figure 20: Simulated longitudinal thermal and optical intensity gratings are shown above from a study in [20]. The loss of phase relation between red and blue gratings at high optical intensity is responsible for mode coupling in MI.....	36
Figure 21: The wavelength dependence of MI threshold is shown above from a study in [21] along with the estimated population inversion curve (green).....	40
Figure 22: A schematic of the counter-pumped amplifier is shown above.....	41
Figure 23: A temporal response of the optical phase modulation sequence for a 1 GHz clock rate, 7 bit pattern PRBS scheme is shown [25].....	44
Figure 24: The power spectral density of an optical signal after PRBS phase modulation with a 7 bit pattern driven at a clock rate of 2 GHz is shown above [26]. The left shows a long-range power spectrum while the right shows a more narrow frequency range with emphasis on the discrete tones comprising the total response.....	45
Figure 25: The output spectrum of the seed due to phase broadening is shown above in the hybrid fiber power scaling experiments.....	46
Figure 26: The pump power versus signal power for the 37/370 μ m diameter core/clad is shown above. The change in response at 900 W pump is due to parasitic beam steering of the pump.....	47

Figure 27: A high-resolution optical spectrum of the backward light is shown above. The spectrum of the 37/370 μm fiber under test is shown with ample Stokes light along with a reference spectrum with no Stokes light.....	48
Figure 28: M2 beam quality versus signal power is shown above. The uptick in M2 at high powers may be a precursor to MI.....	49
Figure 29: The optical-to-optical power efficiency is shown above along with corresponding M2 values.....	50
Figure 30: Individual frames from a high-speed camera showing modal instability.....	51
Figure 31: x- and y-axis M^2 values versus pump power showing MI onset occurred in the y-axis; which is guided by air gaps. Inset: the orientation of the high-index and air gap cladding structures.....	52
Figure 32: The forward OSA trace of the 35.5/355 μm diameter core/clad fiber design is shown above. The high levels of ASE centered at 1040 nm caused a self-pulse that catastrophically damaged the fiber.....	53
Figure 33: The amplified signal versus launched pump is shown above for the Clemson PBGF. The original power scaling data is shown in black while the replication study is shown in blue. Markers indicate the onset of MI in each case as evidenced by the rapid increase in M^2	56

1. Summary

This research addressed suppression of stimulated Brillouin/Raman scattering in high power fiber lasers. The work was done by Mr. Cody Mart under a government research grant. Dr. Ben Pulford provided expert mentorship and laboratory space at the Air Force Research Lab (AFRL) New Mexico. Mr. Mart successfully defended his dissertation using the results reported herein. The principal achievements were:

- Record output power from a ytterbium-doped photonic bandgap fiber amplifier (410 W, 15x improvement), and a hybrid fiber amplifier (820 W, 14x improvement).
- Stimulated Brillouin Backscattering (SBS) behavior studied numerically & experimentally in Photonic Band Gap Fiber (PBGF); simulation results are in excellent agreement with experimental results.
- SBS suppression by core feature demagnification.
- Large mode area Yb-doped microstructured fiber amplifiers shown suitable for further power scaling.
- One PhD student graduated.

2. Introduction

Lasers are used in a wide range of applications that benefit from the tightly focused beam and extremely high intensity that they can provide. In many cases, high average power is essential for material modifications (cutting, drilling, and marking, just to name a few). Fiber lasers have had a dramatic raise in capability over the past decade and the trend is still continuing. The fastest growth in output power was observed for Yb-doped fiber system with an increase in average of almost 2 times each year since the year of 1999. Overall, the output power in Yb-doped fiber lasers has increased by two orders of magnitude in the past decade. This level of development is unprecedented compared to other laser platforms (crystal-based or gas-based). State-of-the art Yb-doped lasers

can be massively scaled to an astounding 10 kW – comparable to the best performance of any developed lasers currently available in the market. The result was obtained with close to diffraction-limited beam quality, which determines the ability to focus to a diffraction limited spot. For that reason, the brightness, which determines the power density achievable on a target, is exceptionally high for these fiber lasers. This is important since the power density largely defines the outcome of the treatment in the majority of applications. Significant progress has also been visible for other fiber lasers operating around 1550nm (Erbium-doped fiber) and around 2000nm (based on Thulium and Holmium gain fibers).

The advances in fiber lasers have not come without the significant amount of research efforts to solve a few obstacles on the road. First, high pump powers are needed to get enough energy into the laser systems. Fortunately, high power laser diodes have been developed in recent years and are available at power levels as high as hundreds of kW with combined laser diode arrays. Second, high output optical powers can lead to optical damage of fibers. The damage threshold of silica is about $50\text{W}/\mu\text{m}^2$. When the optical power inside the fiber is greater than this value, the fiber tends to be damaged. The damage threshold can be lower if care would not be taken to avoid the so-called fiber fuse. Furthermore, due to the strong confinement in fiber geometry nonlinear effects play an important role in high power fiber lasers. Among the nonlinear effects, stimulated Brillouin backscattering (SBS) is the limitation in output power scaling for narrow-band lasers; and stimulated Raman scattering (SRS) can generate frequency shift signals which decreases the output power at the required wavelength. Modal instabilities are another obstacle in power scaling of fiber lasers/amplifiers. To scale up the output power of fiber lasers further we need to use the so-called large mode area fiber designs. These fibers tend to create lower beam quality due to coupling between the fundamental (desirable) and higher order modes (undesirable). Thus, In order to reach the material limit output power of fiber lasers/amplifiers we need to control stimulated Brillouin/Raman scattering and MI effectively.

3. Methods, Assumptions, and Procedures

The extent of this research is to interrogate stimulated Brillouin scattering (SBS) and modal instability (MI) in large mode area Yb-doped microstructured fiber amplifiers. The performance goal of this research was to demonstrate milestones in output power of beam combinable fiber amplifiers with high optical-to-optical efficiencies and with beam qualities that approach the diffraction limit. The choice to study SBS and MI was made because each is the bottlenecking process for narrow-linewidth output power and diffraction limited beam quality respectively.

This work will treat SBS as a bane, as SBS depletes the forward-propagating light of power and has been linked to intensity-induced fusion in active fiber. The focus will be to understand the physics involved and to minimize its effect. It is worth noting, however, that Brillouin scattering in fiber has been utilized for precision measurements including high-sensitivity strain and temperature identification, and as a narrow-linewidth laser source. No technological utility has been derived from MI because it is fundamentally an unstable process, and this work will likewise treat MI as a bane.

The choice for limiting the study to ytterbium-doped fiber amplifiers was made because favorable glass chemistry, favorable energetics in ytterbium, technological advances in 900-1000 nm diode pumping, and photonic component reliability at 1064 nm has engendered a platform for demonstrating impressive power amplification feats in Yb-doped fibers. In a traditional rare-earth (RE) doped fiber amplifier, fiber coupled diode lasers with low spatial coherence are directly coupled to the waveguide containing the signal and the RE dopant, and are tuned to pump a strong absorption line in the RE dopant. The laser signal, tuned to a strong emission line, extracts power through stimulated emission. In this work, the strong Yb absorption line that is pumped is 976 nm and the Yb emission line is 1064 nm. Other RE metals prevalent in near IR silica fiber amplification development were neglected for power scaling in a master oscillator power amplifier (MOPA) configuration because each suffers from some, but not all, of the following deficiencies: low optical-to-optical efficiency, high quantum defect heating, low solid solubility limits in silica fiber, losses to non-radiative recombination processes such as homogenous up-conversion in Erbium, and operation in the high-silica-loss spectral region (relative to 1550 nm) such as thulium and holmium.

This work will study fiber amplifiers and neglect fiber lasers. A fiber laser differs from an amplifier in that the waveguide contains optical cavity feedback and is not seeded with laser signal. Instead, stimulated emission from the peak of the rare-earth (RE) dopant emission oscillates in the fiber. Reflections for the oscillator can rely on the ~4% Fresnel reflection at the air/glass interface or on external mirrors to provide feedback. The primary reason that fiber lasers will be neglected is that control of the frequency linewidth is important for both SBS mitigation and for coherence length considerations in beam combining architectures. The requirements for a fiber laser to be high power with a controllable, narrow linewidth when pumped by low-brightness diodes are contradictory whereas these can be achieved cooperatively in a fiber amplifier. The length of the gain fiber is the primary source for contradictory demands on a fiber oscillator in that long lengths are needed to achieve high absorption and thereby achieve high optical-to-optical efficiency whereas short lengths are needed to maintain single longitudinal mode behavior from the oscillator and maintain a narrow-linewidth and jointly mitigate SBS. A fiber amplifier, in contrast, can utilize long lengths (on the order of 10 m) and achieve high efficiency because the frequency linewidth of the master oscillator can be deterministically broadened before seeding the final stage amplifier. Intensity noise, defined as the temporal fluctuations in output power, is also notoriously bad in fiber lasers compared to semiconductor and solid-state lasers, but is ameliorated in MOPA architectures because low-intensity-noise seed sources can preserve the low intensity noise in fiber amplifiers relative to fiber lasers.

The research presented in this report is a collaborative effort between the University of Arizona, College of Optical Sciences and the Air Force Research Laboratory (AFRL) Fiber Lasers and Beam Combining Group, with the entirety of the research being conducted at AFRL under the auspices of an Educational Partnership Agreement. Computational resources were needed to model SBS in microstructured fiber. This research will be presented in the section below. The Department of Defense High Performance Computer consortium was utilized for these large computations.

4. Results and Discussion

4.1 Experimental and Theoretical Investigations of Stimulated Brillouin Scattering

In this chapter, a Pump Probe Brillouin Gain Spectrum (BGS) diagnostic tool is used to measure acoustic properties and to estimate SBS threshold in commercially-available fibers as a proof-of-concept and in the novel microstructured fibers of interest for this dissertation. The first section is devoted to understanding SBS in optical amplifiers. The second section is devoted to understanding Pump Probe theory and practice, and a commercially-available 6/125 μm core/clad passive, polarization maintaining Germania-doped fiber is used for validation. In the third and fourth sections, the BGS of the microstructured fibers used in later power scaling experiments are presented

In the final section, the experimental values for g_B are tested against a theoretical treatment of the acoustic-optical wave coupling that estimates g_B with a finite element solver. Brillouin coupling in a core with non-uniform acoustic velocity profile is numerically investigated by solving a non-homogenous Helmholtz equation describing the acoustic displacement in the core material driven by the optical field.

4.1.1 SBS Theory

A. Mathematical and Physical Description

SBS is a 3-wave nonlinear optical process involving an incident wave, an acoustic wave, and a scattered wave. As the incident field passes through the waveguide, a density wave is generated through a process known as electrostriction in response to high-intensity, counter-propagating electric fields. Light is scattered from the density wave, and in the process emits a phonon to satisfy conservation of energy and momentum. The phonon is phase-matched to take on a wave vector twice of that of the pump guided wave propagation constant because the Stokes light propagation is opposite of the incident pump. The relevant fields and directions are shown in figure 1. The phonon modifies the material density in a wave-like manner as it propagates, and accordingly modifies the refractive index. This propagating density field can be viewed as a reflective Bragg structure, and is essentially stationary in a timeframe that the

optical wave propagates through the fiber. Pump light scatters from the traveling wave Bragg structure and emits more phonons in the process. The buildup of scattered, or Stokes, light is phenomenologically modeled as an exponential process as the buildup of Stokes light emits phonons and phonons create scattering sites to generate more Stokes light.

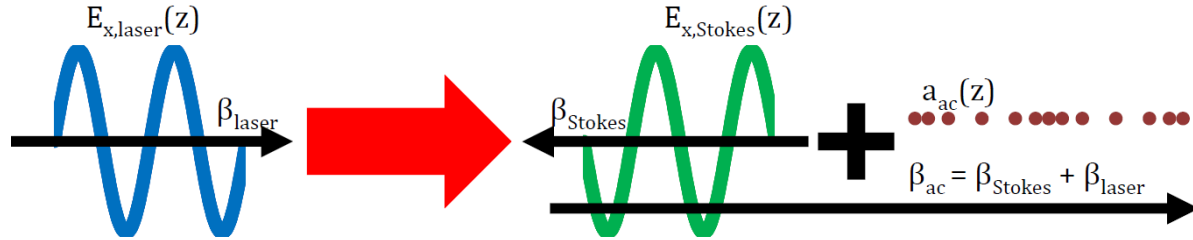


Figure 1: The two interacting optical fields and the acoustic wave are shown schematically along with direction of propagation. The laser field polarized in the x-direction, $E_{x,laser}$ scatters to form the optical Stokes field, $E_{x,Stokes}$, and an acoustic displacement, a_{ac} .

SBS onset in low-loss passive fiber has been considered theoretically for conventional long-haul optical communications systems carrying short pulses of information [1]; which results in a closed-form solution for the SBS threshold. The seeding mechanism for SBS in that case was purely from spontaneous Brillouin scattering due to interactions with thermally-generated acoustic waves. In an optical amplifier, however, ASE that is generated within the BGS can seed the SBS process as well. In addition, the Stokes light will amplify due to both Brillouin scattering and optical gain while the forward pump light is amplified.

The governing equations below, as modeled in [2], are written in a frame of reference such that $z = 0$ is the fiber facet in which the pump and signal are co-seeded and $z = L$ is the output end of the fiber. The Stokes light is amplified in the $-z$ direction. Background attenuation is neglected because of the short lengths (~ 10 m) and low inherent losses of rare-earth doped fiber while being pumped on a strong optical transition.

The evolution of the pump, laser, Amplified Spontaneous Emission (ASE), and Stokes powers (P_P , P_I , P_{ASE} , P_S) are modeled in equations (1)-(5) below. The pump excites electrons to the upper state, N_2 , and provides inversion for all other signals. The laser

extracts power due to stimulated emission and loses power due to Brillouin coupling to the Stokes light. The Brillouin coupling is represented by the $P_s \times P_l$ term. The Stokes light is amplified through stimulated emission and nonlinear Brillouin coupling. In the co-pumped configuration, as is the case below, the Stokes light will have its highest fields present at the $z = 0$ boundary of the fiber where the highest levels of inversion are present because the Stokes is counter-propagating with the pump. In contrast, the laser will have weak optical fields at the $z = 0$ end and will amplify towards the $z = L$ end of the fiber because the pump and laser signals co-propagate along the fiber. This means that Stokes light can compete favorably for optical gain near the $z = 0$ boundary because power extraction from population inversion depends on local field intensities.

$$\frac{d}{dz} P_p = \Gamma_p P_p (N_2 \sigma_p^e - N_1 \sigma_p^a) \quad (1)$$

$$\frac{d}{dz} P_l = \Gamma_S P_l (N_2 \sigma_l^e - N_1 \sigma_l^a) - P_l \sum_i g_{B_i} P_{S_i} / A_{eff} \quad (2)$$

$$\pm \frac{d}{dz} P_{ASE_j}^{f,b} = \Gamma_S P_{ASE_j}^{f,b} (N_2 \sigma_{ASE_j}^e - N_1 \sigma_{ASE_j}^a) + \Gamma_S N_2 \sigma_{ASE_j}^e P_{0_j} \quad (3)$$

$$\frac{d}{dz} P_S = -\Gamma_S P_S (N_2 \sigma_S^e - N_1 \sigma_S^a) - P_l \sum_i g_{B_i} P_{S_i} / A_{eff} \quad (4)$$

$$N_2 = N_0 \frac{\Gamma_S \sigma_S^a P_S \lambda_S + \Gamma_p \sigma_p^a P_p \lambda_p + \Gamma_S \sum_j \sigma_{ASE_j}^a P_{ASE_j}^{f,b} \lambda_{ASE_j} + \Gamma_S \sum_j \sigma_S^a P_S \lambda_S}{\Gamma_S \sigma_S^e P_S \lambda_S + \Gamma_p \sigma_p^e P_p \lambda_p + \Gamma_S \sum_j \sigma_{ASE_j}^e P_{ASE_j}^{f,b} \lambda_{ASE_j} + \Gamma_S \sum_j \sigma_S^e P_S \lambda_S + hc A_{eff} / \tau} \quad (5)$$

In this model, the excited state ion density, N_2 , is described by stimulated emission and absorption rates of all contributing signals and the spontaneous decay rate with inverse fluorescence lifetime $1/\tau$. The two-level approximation of the excited- and ground-state populations are assumed as in the steady-state and N_0 is the sum of ground and excited states. The emission/absorption cross sections of the ytterbium-doped fiber at each wavelength of interest are $\sigma^{a/e}$. To model the effects of imperfect pump overlap with the core and the optical field distribution of the core mode, the overlap factors Γ_S and Γ_P are introduced. The forward and backward ASE, superscripts f and b , is discretized with parameter j to cover the spectrum with j lines, and is simulated with a boundary condition fictitious seed of $P_0 = (2hc/\lambda_{ASE}) \cdot \Delta U_{ASE}$ where ΔU_{ASE} is the ytterbium gain bandwidth. The Brillouin gain is similarly discretized with index i , and the

gain coefficient, g_B , is assumed to take a lorentzian line shape with bandwidth Δu_B and peak value g_{B0} . The fictitious seed at $z = L$ of the Stokes light is given as $P_N = h\nu_B\Delta\nu_B$ where u_B is the Brillouin peak shift, and is designed to simulate phonon generation from noise [3].

B. SBS Mitigation Through Clever Amplification Schemes

SBS mitigation through different optical gain configurations has been discussed, and now will be expounded on. Specifically, minimizing the total integrated power along the fiber length is beneficial to SBS mitigation. Two examples of utilizing favorable optical gain are counter-pumping and the so-called two-tone amplifier configuration. Basic fiber amplifier schematics for a co-pumped, counter-pumped, and two-tone amplifier are shown in figure 2. The pumps in the figure refer to lasers tuned to excite an optical transition in a rare-earth dopant, and not to the pump used to excite an SBS process. The role of the intermediate laser in the two-tone amplifier will be discussed below.

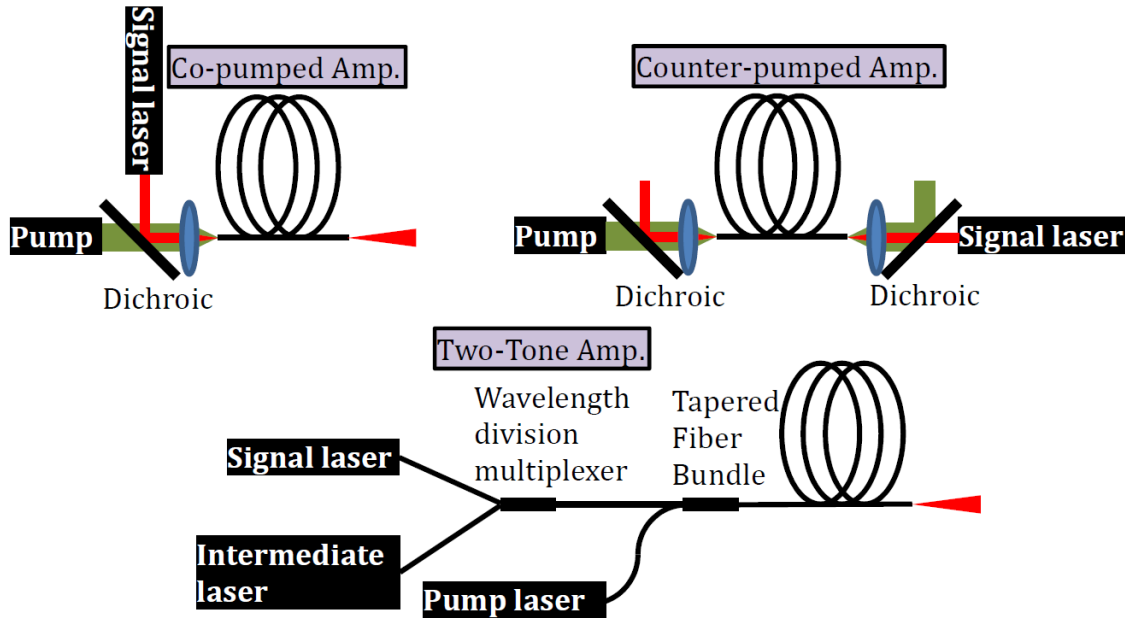


Figure 2: Fiber amplifier schematics for co-pumped, counter-pumped, and two-tone configurations are shown. In the two-tone schematic, a wavelength division multiplexer is a photonic component that couples two fibers of differing wavelengths in the same fiber core. A tapered fiber bundle evanescently couples multimode fibers into the cladding mode of a double-clad fiber

From the coupled equations above, it is evident that the population inversion is similar to a Beer's law decay with length. It is also evident that the local laser gain along the

fiber is affected by population inversion, i.e. $\frac{dP_l}{dz} \sim N_2 \times P_l$. This term in the differential equation also implies power extraction from stimulated emission at any point z depends on the local laser intensity along the fiber. In a counter-pumped amplifier, the laser signal is highest at a point of the fiber where the highest inversion levels are present. In contrast, a co-pumped amplifier has weak laser fields present at the highest inversion levels. This creates vastly different power evolution profiles along the fiber axis; which is simulated in figure 3. In the figure, the co- and counter-pumped amplifiers reach the same output power. The co-pumped amplifier, shown in red, maintains high power levels through much of the latter half of the fiber as opposed to the counter-pumped amplifier, shown in blue; which rapidly extracts power at the output end of the fiber. This means that throughout much of the fiber low optical fields exist in the counter-pumped case. These low optical fields do not strongly excite the electrostriction process because the process relies on localized field strengths to order $E_x(z)^2$. That much of the fiber in a counter-pumped configuration maintains low optical fields locally is the reason SBS threshold is increased in counter-pumped fiber amplifiers [2].

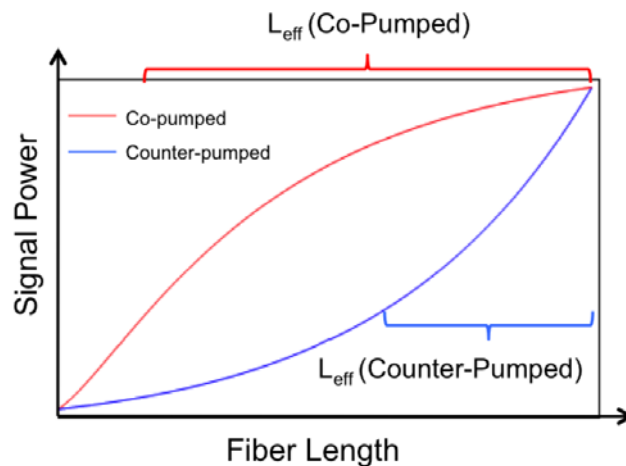


Figure 3: The evolution of the laser signal along the length of the fiber in a co-pumped (red) and counter-pumped (blue) amplifier configuration are shown above

A two-tone amplifier is a pumping scheme that similarly reserves much of the laser amplification to a small section of the fiber, but with the exception that the effect can be

seen in co-pumped configurations [4]. In the two-tone scheme, a ytterbium-doped large-mode-area (LMA) fiber core is seeded with the signal and an intermediate laser at a wavelength near the peak of the emission spectrum of ~ 1035 nm whose role is to quickly amplify and get re-absorbed to act as a second pump to the intended signal. The simulated power evolution of the intermediate and signal lasers along the length of the fiber in a two-tone amplifier is shown in figure 4 as described in [5]. In the figure, power was scaled until SBS threshold was met. The intermediate laser, shown in green, dominates power extraction at the $z = 0$ seeded boundary until it is reabsorbed and thereby provides gain for the signal, shown in blue. Since the intermediate laser is a core mode, absorption is high and amplification of the signal occurs in a very short section toward the end of the fiber. Also shown in the figure is a simulated co-pumped amplifier with only a 1064 nm seed, shown in red. Since both the two-tone and single-tone amplifiers were pumped until the SBS threshold was observed, it can be inferred that the two-tone configuration amplified a 1064 nm laser signal $>2\times$ beyond the SBS threshold of a single-tone amplifier.

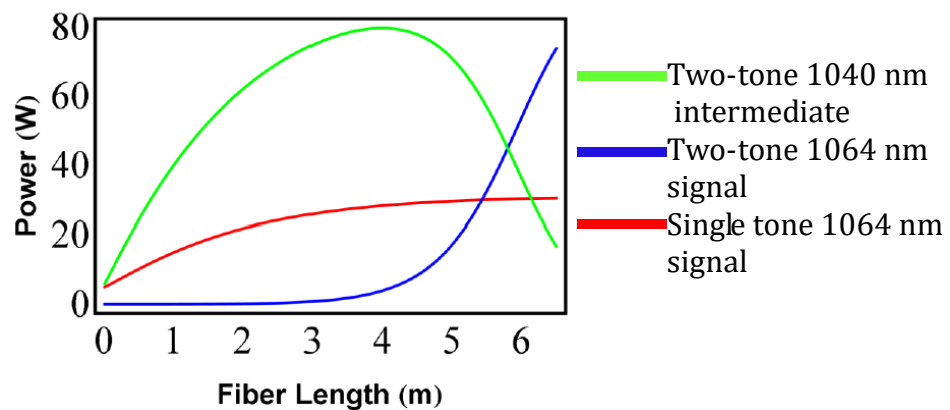


Figure 4: The evolution of the laser signal along the length of the fiber with a single laser at 1064 nm (red) is shown with a two-tone amplifier with an intermediate laser at 1040 nm (green) and signal laser at 1064 nm

4.1.2 Pump Probe Theory

A. Introduction and Mathematical Modeling

In Pump Probe BGS measurement, opposing ends of the fiber are seeded with simulated pump and Stokes (probe) light that are detuned in frequency, thus creating a longitudinal interference pattern mimicking an acoustic wave in the fiber core. When the laser field interference pattern matches the grating formed by the acoustic wave, maximum power coupling through the Brillouin scattering process is achieved. The spectrum of interacting acoustic waves in the fiber can be determined by the strength of the energy coupling as a function of frequency detuning between the pump and probe. It differs from spontaneous Brillouin scattering in that the Stokes light is seeded from a laser and not scattered from thermal phonons.

Pump Probe BGS offers many favorable advantages over monitoring Stokes light in an active amplifier. A response can be observed at pump powers below the saturation power of the rare-earth doped fiber, thus the natural g_B can be obtained with no ambiguities as to the role of signal attenuation in the process. Also, no temperature gradients along the fiber exist in this setup; which can be observed in active amplifiers due to quantum defect heating.

Two varieties of Pump Probe BGS have been widely implemented: a dual-source (DS) scheme [6] in which two independent lasers are frequency detuned, and a phase modulator (ϕ -mod) method [7] in which a single-source is split and the probe is phase modulated to create interacting frequencies in the ± 1 tones of a phase modulator driven by a sinusoid. Figure 5 shows a schematic of the frequency content in the dual-source and phase modulator methods along with the power coupling involved. In the phase modulator method, the phase modulator is driven with a single sinusoid at a drive voltage that depletes the center frequency content to zero. This is done to prevent stimulated Rayleigh scattering and other same-frequency processes from interacting in the fiber. The phase modulator method involves a 2-level interaction scheme in which the +1 tone of the phase modulator amplifies the pump; which then amplifies the -1 tone. The DS is much simpler in that interaction only involves the pump amplifying the probe.



Figure 5: Pump and Probe power coupling schematics for the dual-source (left) and phase modulated (right) BGS methods are shown

Advantages of the ϕ -mod method are that the error in the frequency difference is lower and can be controlled at the resolution of the radio-frequency (RF) drive source, and the measurement is not subject to the slow frequency drift of the laser. The advantage of the DS method is that the 2-level interaction only engenders gain for the probe and loss for the pump. The 3- and 2-level governing equations that describe the Brillouin coupling in the ϕ -mod and DS methods are given below in equations (6)-(8) for ϕ -mod and (9)-(10) for the DS [8].

Phase Modulation Governing Equations

$$\frac{d}{dz} P_{s+}(z) = -\frac{g_B}{A_{eff}} P_p(z) P_{s+} - \alpha P_{s+}(z) \quad (6)$$

$$\frac{d}{dz} P_p(z) = -\frac{g_B}{A_{eff}} P_p(z) (P_{s-}(z) - P_{s+}(z)) + \alpha P_p(z) \quad (7)$$

$$\frac{d}{dz} P_{s-}(z) = \frac{g_B}{A_{eff}} P_p(z) P_{s-} - \alpha P_{s-}(z) \quad (8)$$

Dual Source Governing Equations

$$\frac{d}{dz} P_p(z) = \frac{g_B}{A_{eff}} P_p(z) P_s(z) + \alpha P_p(z) \quad (9)$$

$$\frac{d}{dz} P_s(z) = \frac{g_B}{A_{eff}} P_p(z) P_s(z) - \alpha P_s(z) \quad (10)$$

Here, the frame of reference is at the output end of the fiber, and equations are propagated from $z = 0$ to $z = -L$ for a fiber of length L . In equations (6)-(8), $P_{s+/-}$ is the probe power in the $+/-$ 1 tones of the phase modulator. P_p is the pump power, A_{eff} is the effective fiber mode area and is generally approximated as the circular area of the mode field diameter. The small-signal Brillouin gain coefficient is given by g_B . The attenuation coefficient is given by α and is assumed to be constant for each field. In the 2-level system, the terms remain the same with the exception that the total probe power is

encompassed in P_s . These governing equations do not contain gain/loss terms due to ytterbium population inversion because the Yb absorption at 1064 nm does not supply sufficient population inversion to have an effect.

In the absence of attenuation, the pump and probe power equations can be solved analytically. Solutions for the lower tone of the ϕ -mod, Eqn. (8), and the Stokes light in the DS, Eqn. (10), are given in equation (11) and equation (12), respectively. The solutions represent a co-seeded initial condition in which the pump and Stokes power incident on the fiber are known. This does not accurately model SBS in that the process is counter-seeded. In the case of counter-seeding, the solution becomes transcendental. These exact solutions for the co-seeded condition, however, were useful in estimating the numerical error when finite difference methods were used to estimate the power coupling in the 3x3 and 2x2 coupled differential equations above with $\alpha = 0$. Ultimately, estimating the numerical error was necessary because the microstructured fibers studied below have non-negligible attenuation due to Yb absorption and scattering, and using finite difference methods to estimate the power exchange in Eqns. (6)-(8) and (9)-(10) offered the most facile method for simulating the power coupling. It was found that for Δz steps along the fiber to order $\Delta z/L \sim 10^{-6}$, a difference between exact and approximated power amplification was $\sim 0.1\%$; which is smaller than the error in measuring the power in the actual experiment.

Phase Modulation Lower Probe Tone Solution

$$P_{s-}(L) = \frac{-P_t}{2} + \frac{\sqrt{P_t^2 - 4P_{s-}(0)P_{s+}(0)}}{2} \frac{1 + \exp\left[\frac{g_B}{A_{eff}} \sqrt{P_t^2 - 4P_{s-}(0)P_{s+}(0)} L + C'\right]}{1 - \exp\left[\frac{g_B}{A_{eff}} \sqrt{P_t^2 - 4P_{s-}(0)P_{s+}(0)} L + C'\right]} \quad (11)$$

Dual Source Probe Solution

$$P_s(L) = \frac{P_p(0) - P_s(0)}{\frac{P_p(0)}{P_s(0)} \exp\left[\frac{-g_B(P_p(0) - P_s(0))L}{A_{eff}}\right] - 1} \quad (12)$$

where the initial conditions on the ϕ -mod equations are $P_t = P_p(0) - P_{s-}(0) - P_{s+}(0)$ and

$$C' = \ln \left[\frac{2\sqrt{P_{s-}(0)P_{s+}(0)} + P_t - \sqrt{P_t^2 - 4P_{s-}(0)P_{s+}(0)}}{2\sqrt{P_{s-}(0)P_{s+}(0)} + P_t + \sqrt{P_t^2 - 4P_{s-}(0)P_{s+}(0)}} \right]$$

B. Estimations of g_B

Estimates of the g_B were obtained by using finite difference methods to solve the coupled equations (6)-(8) for the ϕ -mod or (9)-(10) for the DS method, and tuning g_B in the equations to match the simulated power results with the acquired data. The boundary conditions for the simulation were empirically derived from the experiment. Figure 6 shows a schematic of the amplified probe and depleted pump BGS that shows the power levels used as boundary conditions in the simulations. When the frequency difference is far off Brillouin resonance, no Brillouin coupling occurs, and the power

dynamics evolve as $\frac{dP_{p/s}}{dz} \sim \pm \alpha P_{p/s}$ because only fiber attenuation affects propagation. With these power measurements, the powers coupled to the waveguide can be estimated and power levels for the boundary conditions $P_p(L)$ and $P_s(0)$ can be defined. When strong Brillouin coupling occurs, power evolves according to the governing equations above and peak interactions can be used to determine $P_p(0)$ and $P_s(L)$. This provides the four boundary conditions for the simulations to match. By power-tuning the pump, g_B can be estimated for a spectrum of pump powers and a statistical average can be utilized to judge the quality of the estimation.

4.1.3 Comparison of Dual Source and Phase Modulator Systems: Phase Modulator System and Results

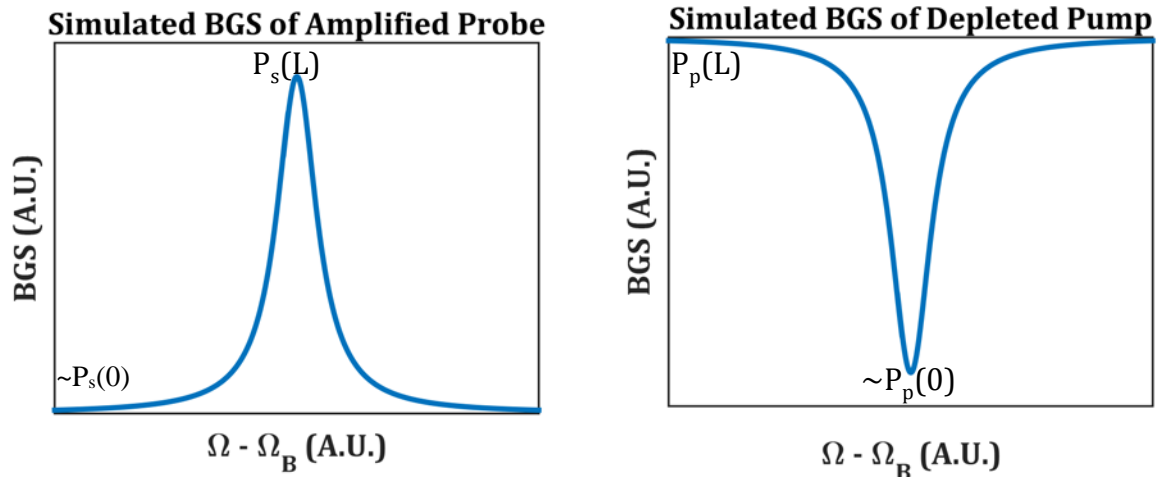


Figure 6: Simulated BGS for amplified probe and depleted pump are shown along with locations of the boundary conditions used for numerical simulations

The first experiment conducted was to determine which of these methods was suitable for BGS measurements for low Brillouin gain conditions such as short fiber length and/or large diameter cores. A short (3.6 m) length of passive, polarization maintaining, single clad GeO₂ doped 6/125 μm core/clad fiber from OFS (product number F9920-01) was chosen for the study. The experimentation and results of the ϕ -mod system will be discussed in this section with the DS experimentation and results discussed in the next section.

In the ϕ -mod schematic, shown in figure 7, a master oscillator (M.O.) is split with a polarization beam splitter (P.B.S.). The pump is coupled directly to an all-fiber high power, single-frequency Yb-doped amplifier from IPG photonics. The probe is coupled to a LiNbO₃ waveguide phase modulator from EOSpace and is driven by a 20 GHz RF driver from Anritsu. The output is coupled into another IPG photonics amplifier to offer mild amplification beyond the ~ 20 mW maximum that can be coupled to the phase modulator without damaging the unit. The output of each amplifier is sampled with a beam splitter (B.S.) to test source stability. Two power meters (P.M.) are dedicated to measuring source stability and two power meters are used to measure the power coupling of the transmitted pump and probe beams. Free-space Faraday isolators are

used to prevent seeding the amplifiers with backward propagating light. Beam samplers are also used to directionally separate the pump and Stokes light in the free-space section of the diagnostic system. It should be noted, however, that in the experiments of the LMA microstructured fiber the 70/30 and 50/50 beam splitters were removed because high powers were needed to elicit a response from those fibers. The IPG amplifier is a 3-stage amplifiers, and the powers needed to measure high fidelity signal ($< 3 \text{ W}$) would not require activation of the third stage in the IPG Amp. The beam splitters were utilized to attenuate the seed beams so that the third stage would need to be active, as this was found to reduce intensity noise of the sources.

To couple light to the fiber in this system and the DS system discussed below, a simple ABCD ray tracing matrix algorithm was used to simulate the propagation of a Gaussian beam through a doublet lens system. The targeted optical design was achieved when the simulated ray path achieved a beam waist that was equal to the mode field diameter of the fiber. In this study, short focal length lenses ($f < 8 \text{ mm}$) were needed to mode-match due to the small core diameter; which necessitated use of specialty glasses whose thermo-optic effects greatly influence focal length. In studies on the microstructured fiber, longer focal length lenses made from UV-grade fused silica were used; which reduced these parasitic thermo-optic effects.

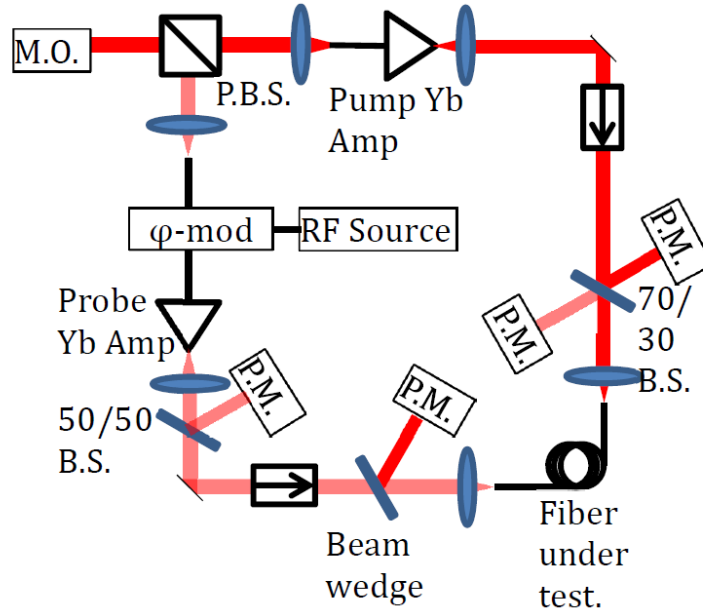


Figure 7: A pump probe design schematic for the phase modulator system is shown

Data was acquired in the ϕ -mod experiment using a LabVIEW code that controlled the RF drive voltage and frequency to the phase modulator to maintain the desired frequency content in the probe while also controlling the IPG output power and recording the power meter levels. Prior to acquisition, the transmitted power was measured in the pump and probe beams so that the data could be calibrated to represent the power in the fiber. Data acquisition was long (>10 minutes per sweep) and was limited by the response time of the thermal power meters that were used to measure powers > 200 mW. The response time for the LabVIEW code to properly acquire data from the power meters took ~ 500 ms for each datum, and many data were taken at each temperature setting so that averaging could be used to acquire high-resolution data.

Figure 8 shows the measured BGS of the OFS test fiber using the ϕ -mod method. The measured full-width at half-maximum is 40 MHz. The peak response at 15.8 GHz is characteristic of germania doping [7]. The pump power coupled to the core is listed in the inset. The importance of this will be discussed later in this chapter because the same power was used to measure the BGS in the DS system and additional features were resolved. Additionally shown in the figure is the estimated g_B vs a range of pump powers. The average was $g_B = 1.6 \times 10^{-11}$ m/W. Notice the wide fluctuations in estimated

g_B at low pump powers. This significantly increased errors as evidenced by the standard deviation; which was 0.1×10^{-11} m/W.

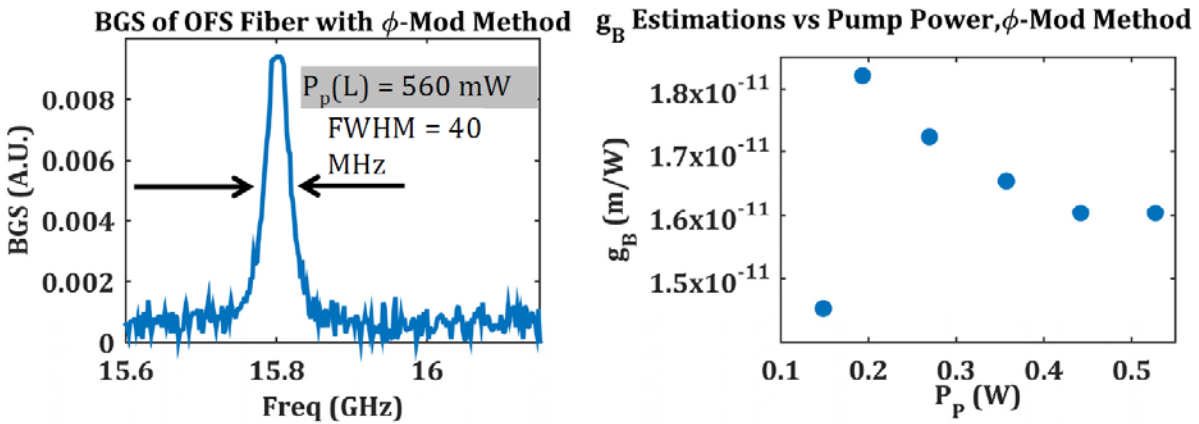


Figure 8: Brillouin Gain Spectra for the OFS fiber using the phase modulator method along with the estimated g_B at a range of pump powers tested

4.1.4 Comparison of Dual Source and Phase Modulator Systems: Dual Source System and Results

The DS system, shown in figure 9, is the same following the IPG amplifiers as the ϕ -mod system. Where it differs is the implementation of two independent sources to seed the IPG amplifiers. In the DS system, the outputs from two non-planar ring oscillators (NPROs), from Lightwave, are each split using a PBS with the transmitted beam being used to seed the amplifiers and the reflected beam being fiber coupled into a 3 dB coupler. The 3 dB coupler is then used to illuminate a 26 GHz InGaAs photodiode from Newport for heterodyne detection. A radio frequency spectrum analyzer (RFSA) is used to detect the frequency difference between pump and probe. The other fiber from the 3 dB coupler illuminates a scanning Fabry Perot interferometer (SFPI) to analyze the single-frequency behavior of each NPRO. The SFPI interference fringes are read on an oscilloscope. Frequency detuning is achieved by temperature tuning of the NPRO laser crystal. The SFPI is needed to monitor each NPRO for single-frequency output while the probe is frequency scanning. When properly tuned, the probe laser can scan >5 GHz without mode-hopping, or switching between longitudinal modes of the laser cavity, becoming problematic

The DS system needed further characterization because it is the more complex system. Since the laser gain is modified with temperature, a change in the NPRO output power is expected when temperature tuning. Since two NPROs are utilized for the DS system, the NPRO with the lower sensitivity to output power drift while temperature-tuning would be the probe NPRO. A LabVIEW program was written to control the laser crystal temperature and record the NPRO output power from a power meter. Power increases were nearly linear with temperature change. The better performing NPRO decreased power by 8.7% over 23 °C whereas the worse performing NPRO increased 8.2% over 2.9 °C.

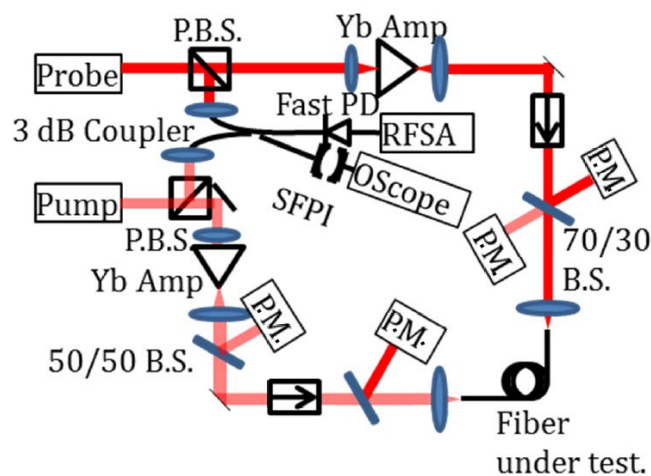


Figure 9: A pump probe design schematic for the dual source system is shown

To understand how the DS system may be affected by the temperature tuning, the better performing NPRO was coupled into a 10 GHz free spectral range Fabry Perot interferometer. A LabVIEW program was written to record the spectral shift in the SFPI when temperature was increased. It was determined that a 1.5 °C temperature increase shifted frequency by 5 GHz. Since most BGS resonances fall within a 2 GHz window between 15 and 17 GHz, it was concluded that the DS system would vary in power <1% due to heating of the crystal.

Data was acquired in the DS experiment using a LabVIEW program that thermally tuned the probe laser and controlled the IPG output power while simultaneously recording the power levels of each power meter and the frequency difference in the

RFSA. This LabVIEW code similarly was slow in data acquisition and was limited by the response time of the thermal power meters.

Figure 10 shows the measured BGS of the OFS test fiber using the DS method. The measured full-width at half-maximum is 60 MHz. The peak response is similarly at 15.8 GHz. As mentioned above, an additional feature is clearly resolved at 16.3 GHz when pumped with 0.56 W. This is due to silica from the evanescent light in the two modes interacting. This is generally a difficult feature to resolve in BG spectroscopy. Also shown is the estimated g_B vs pump power for the DS method. The average was $g_B = 1.61 \times 10^{-11}$ m/W and the measured variance was 0.018×10^{-11} m/W. The variance is much lower in the DS method than in the ϕ -mod method.

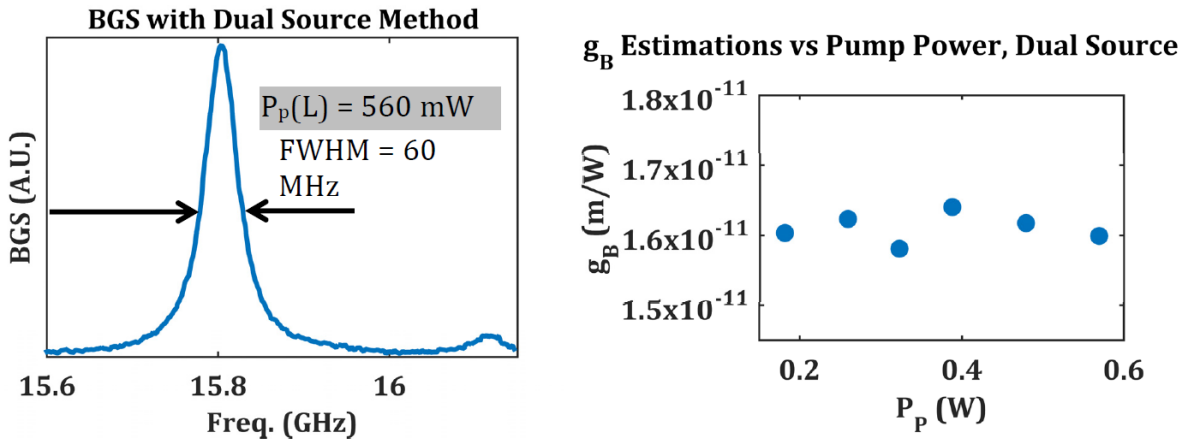


Figure 10: Brillouin Gain Spectra for the OFS fiber using the dual-source method is shown along with the g_B estimated vs pump power

Table 1

Measured Stokes gain and estimated g_B are listed for pump powers in DS and ϕ -

Dual Source Method					Phase Modulator Method				
$P_P(L)$ (W)	0.181	0.259	0.322	0.478	$P_P(L)$ (W)	0.187	0.264	0.351	0.499
$\frac{Ps(L)}{Ps(0)}$	1.387	1.598	1.769	2.337	$\frac{Ps(L)}{Ps(0)}$	1.052	1.095	1.158	1.316
g_B (cm/GW)	1.603	1.623	1.587	1.617	g_B (cm/GW)	1.821	1.7232	1.655	1.604

A. Comparison of Dual Source and Phase Modulator Systems: Discussion

The measured FWHM of the BGS with the DS system was 60 MHz and was 40 MHz in the ϕ -mod system. This large discrepancy in the measured widths is not due to frequency resolution of each measurement system. The DS method resolution is limited to frequency drift of the two sources. The frequency drift measured over a 10 second span is approximately 2 MHz. The ϕ -mod frequency resolution is much more precise. The resolution limit is nominally limited by the instantaneous linewidth of the NPRO; which is rated at 10 kHz. This was not detected when inspected because the resolution limit of the system was lower than our analysis method of measuring the variations in the beat-note on a fast photodiode. The cause for the large discrepancy in full width at half maximum (FWHM) measurements will be explained later in this section.

Table 1 shows the overall probe gain and estimated g_B for each pump power using the ϕ -mod and DS methods. The overall probe gain is much smaller for a given pump power in the ϕ -mod method. The low signal gain in the ϕ -mod method is the predominant cause for the wide statistical variation in g_B cited above because of the low signal-to-noise ratio (SNR). The large SNR in the DS method is responsible for the lower statistical variation of ± 0.01 cm/GW. The peak Brillouin gain value of 1.6 cm/GW is on the low end for GeO₂-doped fiber cores. This is potentially due to gain saturation effects because of the large pump powers involved.

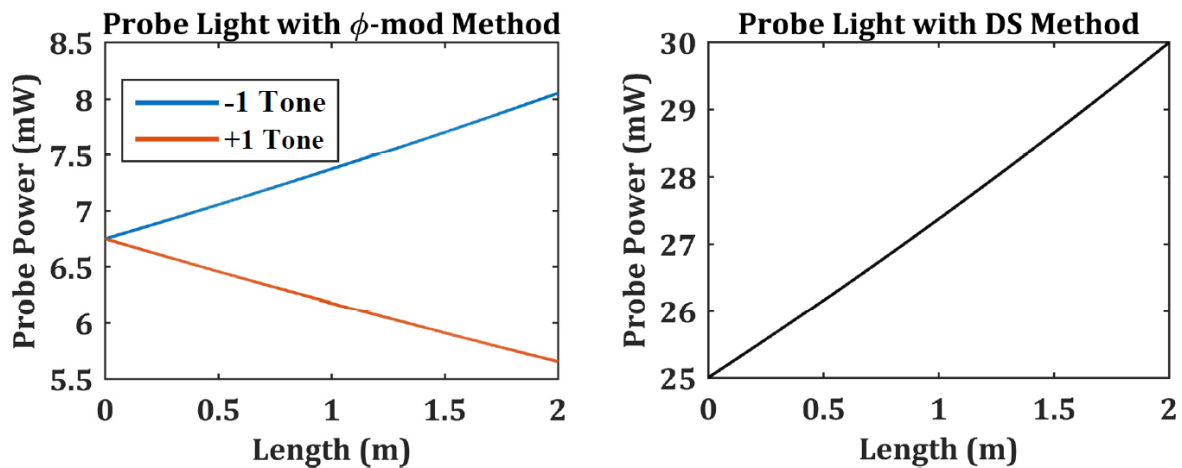


Figure 11: Brillouin Gain Spectra for the OFS fiber using the dual-source and phase modulator methods are shown above. Each is pumped with the same power

To investigate the cause for the abnormal performance of the ϕ -mod method, equations 3.6-3.8 and equations 3.9-3.10 were separately solved using finite difference methods to show the power growth/decay along the fiber. The parameters in the simulation had a similar g_B and effective area as the OFS fiber used in the experiment. Figure 11 shows the power dynamics of the ± 1 tones of the phase modulator along with the probe light in the DS method for the simulated OFS fiber with a pump power of 250 mW and a total probe power of 25 mW. For the ϕ -mod method, the +1 tone loss nearly equals the -1 tone gain for low Brillouin gain conditions. Additionally, of the total probe power only ~54% of the light interacts with the pump because the remaining light is dispersed among higher order tones of the phase modulator. This results in an overall probe gain that is very low compared to the DS method; in which all probe light is amplified by the pump. The total probe power gains in the figure are 1.77 dB for the DS method and 0.069 dB for the ϕ -mod method. To achieve a probe gain of 1 dB, nearly 5x more pump power is required in the ϕ -mod method.

For low gain processes such as responses off of the BGS peak or for short length, large core diameter fibers, the ϕ -mod method as-implemented fails to capture all necessary physics. This then explains discrepancy in BGS FWHM cited above because the low Brillouin gain off peak resonance did not stimulate a strong enough power exchange in the ϕ -mod method to produce a detectable signal.

In spite of its systematic simplicity and high frequency resolution, the ϕ -mod system will not be used in this study. However, if diffractive optical elements and/or Fabry-Perot filters with resolution >0.05 nm at 1064 nm can be integrated, the power dynamics of ± 1 tones of the phase modulator can be studied independently and resolution can be improved.

4.1.5 Brillouin Gain Spectroscopy of All-Solid Ytterbium-doped Photonic Bandgap Fiber

To accurately estimate g_B in the PBGF, a fiber-coupled polarization scrambler from General Photonics was integrated into the probe system to scramble the probe. The polarization scrambler iterated through many cycles of π polarization retardation and advance on a sub-nanosecond time scale. The polarization spanned through every

state of polarization on the Poincare sphere on a ns-timescale. On the time scale of a phonon lifetime (~ 10 ns) this can essentially be treated as a source with no polarization fidelity, or with a polarization extinction ration (PER) of 0 dB. Polarization-scrambling was necessary because the non-PM PBGF degrades the polarization of a highly-polarized source to a $PER < 9$ dB, and a randomly-polarized probe can capture interactions of all polarization states of the pump. The degraded polarization affects the analysis in that the observed g_B is a factor of 2 lower than the natural g_B [9]. The estimated gain coefficient from the experiment must therefore be multiplied by 2. The power of this scrambled probe was boosted in a non-P.M. pre-amplifier that produced 1.2 W of power and a PER of < 0.5 dB. The home-built non-P.M. amplifier was necessary because the IPG amplifier required a seed with high-fidelity polarization and will polarize incoming seeds to achieve this. A polarization-scrambled seed presented to the IPG amplifier would produce a pulsed output because the embedded polarizer would fully attenuate the seed when in the opposite polarization of the embedded polarizer is encountered.

To prepare the fiber for test, the fiber tips were cleaved at a $\sim 4^\circ$ angle to prevent parasitic reflections from the glass/air interface from affecting measurements. The fiber tips were inserted in aluminum chucks atop a 5-axis stage for free-space coupling. No attenuation of the pump IPG amplifier was applied and ~ 40 W were used to seed the fiber under test. The fiber was coiled loosely on an optical breadboard with care taken to maintain a constant bend axis throughout the fiber. The breadboard was positioned at a height coincident with the fiber height in the chucks so as to reduce strain on the fiber due to sag. A beam profiler from Thorlabs was utilized to measure beam quality; of which the pump and probe beams emitted beams with $M^2 < 1.3$. This ensured that the measurement was capturing interactions between fundamental core modes of the pump and Stokes light.

The optimized diameter was chosen as 80 μm from an experiment performed prior to BGS interrogation in which a 1.5 m section of the fiber was tested for optimized bend diameter then subsequently used in a cutback experiment to determine fundamental mode loss at 1064 nm. The short section of fiber was ideal for determining the optimum diameter because the mode filtering via the PBG effect can only occur over a short distance. The optimum bend diameter was determined as 80 μm and the cutback experiment determined an estimated loss coefficient of 0.02 m^{-1} (0.086 dB/m).

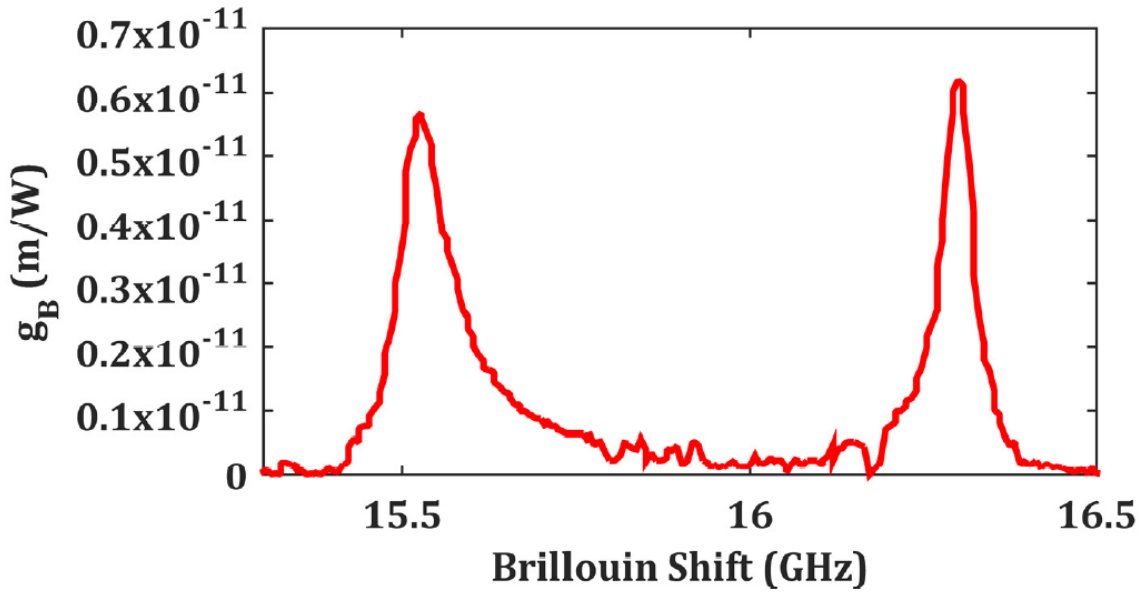


Figure 12: The experimental BGS, scaled to the estimated g_B is shown above

Figure 12 shows the PBGF BGS scaled to the estimated g_B . The two responses are from structures that comprise the core. The 15.5 GHz peak is due to Yb- and P_2O_5 -doped silica and has an estimated g_B of $0.58 \times 10^{-11} \text{ m/W}$. The peak interaction at 16.3 GHz is due to the SiO_2 and carries a magnitude of $0.62 \times 10^{-11} \text{ m/W}$; which is $> 7\times$ lower than g_B for pure-silica cores [7]. Commercial silica fibers have since been corrected for the ultra-high g_B reported in [7], but these still hover around $g_B \sim 2 \times 10^{-11} \text{ m/W}$. The SiO_2 response for the PBGF is at least $3\times$ reduced from these fibers as well. The full-width

and half-maximum bandwidths are 100 MHz for the doped silica region and 80 MHz for the pure silica region. The pure silica bandwidth is nearly twice the bandwidth of traditional step-index fiber. No responses were resolved from the GeO_2 -doped high-index cladding structures responsible for the PBG effect; which would be expected near 15.8 GHz [76]. Acoustic anti-guiding due to interactions with the high-index cladding structures have been proposed as a Brillouin gain suppression mechanism in PBGF [10]. The experimental BGS of the core, however, cannot validate these claims

Even with 40 W of single-frequency pump to couple into the fiber, the measurement was nearing the resolution limits of the diagnostic. This can be seen in figure 13; which shows the g_B that best matched experimental and simulated data for each pump power. The observed g_B was the Brillouin gain experienced in the non-PM fiber. The natural g_B , cited above, is 2x the observed g_B because of the poor polarization fidelity of the PBGF. The spread of optimized g_B values is large compared to the average value, namely an average value of 3.1×10^{-12} m/W for the SiO_2 response with a standard deviation of 2×10^{-13} m/W.

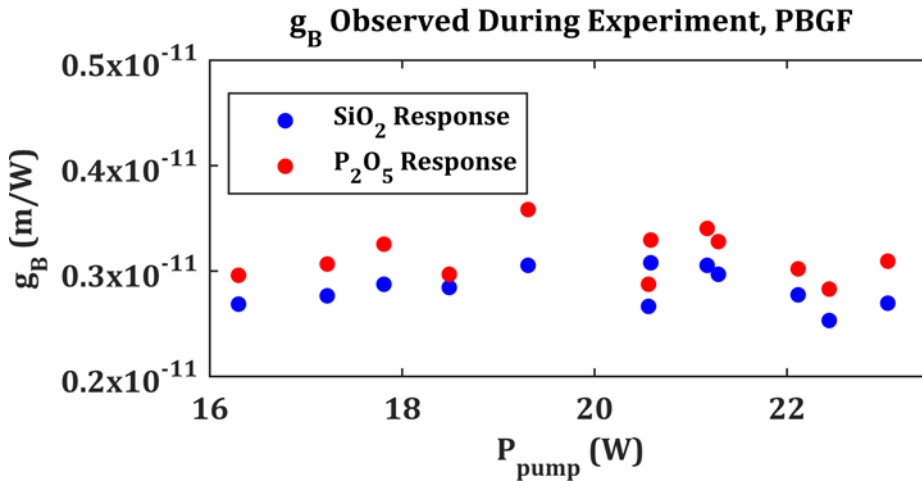


Figure 13: The g_B that best matched simulated and experimental data at each pump power tested is shown above for the PBGF. This data was subsequently scaled to account for effects of a non-PM fiber

The results above do not disprove the conjectures by Shirikawa et al [10] of acoustic wave anti-guiding as a Brillouin gain suppression mechanism because the acoustic wave propagation in the PBGF does not allow for pronounced interactions with the cladding structures. In Shirikawa's study the Brillouin response properties of interest were of a pump wavelength of 1178 nm, a Brillouin peak shift of 14.38 GHz, and a

FWHM gain bandwidth of 56 MHz. These provide an estimated acoustic velocity of 5640 m/s and an acoustic wave lifetime Γ^{-1} of 2.8 ns, with the corresponding propagation distance of 16 μm . This allows for interaction of phonons, if propagating with a transverse component, with the cladding structure because the core radius was 5 μm . The acoustic wave propagation constant was calculated under the assumption of perfect phase matching, i.e. $\beta_P + \beta_S = q$ where $\beta_{P/S}$ are the propagation constants of the Pump/Stokes waves and q is the acoustic wave propagation constant. In the PBGF from Clemson, however, estimated acoustic velocities and propagation lifetimes of the P_2O_5 response are 5686 m/s and 1.59 ns respectively while those of the pure silica response is 5980 m/s and 1.98 ns. These provide a characteristic propagation distance of 9 μm for the P_2O_5 phonons and 11.8 μm for the pure silica phonons. Thus even if PBGF phonon propagation has a transverse propagation component, the majority of the phonons created at the center of the fiber, where the optical fields are highest, will not propagate far enough to interact with the cladding structures because the core radius is 25 μm .

4.1.6 Brillouin Gain Spectroscopy of Hybrid Microstructured Fiber

The NKT hybrid fiber employs annular gain tailoring to mitigate MI. Since the gain tailored core is spatially segregated into active and passive regions, each with a different acoustic response, one might assume that having multiple acoustic frequencies in the Brillouin gain spectrum would increase the SBS threshold. Furthermore, acoustic wave interference between the fundamental core mode and the high index cladding structures as argued by Shirikawa et al [10] would provide a more favorable environment to be observed in the 35 μm core of the hybrid fiber than the 50 μm core of the PBGF since phonon propagation lifetimes would allow for further penetration into the 35 μm core structure. Previous power scaling efforts with Yb-doped hybrid fiber amplifiers did so with broadband seeds and the SBS was not explicitly studied [80]. Hence, studying the Brillouin gain response of this fiber is important to understanding its reliability as a high power fiber amplifier archetype.

The fiber was coiled on a 65 cm diameter aluminum spool with each facet given an angle-cleave of $\sim 4^\circ$. The pump and probe beams were coupled to the core and the transmitted beams maintained a beam quality of $M^2 < 1.2$. The polarization scrambler was again utilized in the diagnostic as the hybrid fiber degraded the pump polarization to a PER < 13 dB.

Two band gap (BG) spectra are shown in Figure 14. The long-range scan on the left shows two distinct responses at 15.9 GHz and 16.3 GHz. The 15.9 GHz feature, which has a measured bandwidth of 42 MHz, corresponds to the response of the Yb-doped center region of the core and the 16.3 GHz feature corresponds to the response from the passive fused silica annulus. To excite a resolvable response from the passive silica, pump powers sufficient to induce pump depletion at the Yb-doped response were needed. Since Yb lowers the BG coefficient in pure silica, it can be inferred that the fundamental core mode overlaps poorly with the pure silica annulus. The natural gain coefficient estimated from the experiment was 1.92×10^{-11} m/W. This is 3x larger than the BG coefficient estimated from the PBGF, but is $\sim 20\%$ smaller than reported traditional LMA ytterbium-doped fibers [2]. During estimations of the BG coefficient, the full mode-field diameter of the core was used to estimate the effective mode area even though the gain-tailored core was not ytterbium-bearing throughout. The 20% reduction in the BG coefficient is therefore ascribed to the presence of the annular pure silica ring in the core. As with the PBGF, no resolvable responses were observed at the GeO_2 -doped glass Brillouin shift frequency of 15.8 GHz indicating that acoustic waves in the high-index cladding rods were not affecting acoustic properties in the core.

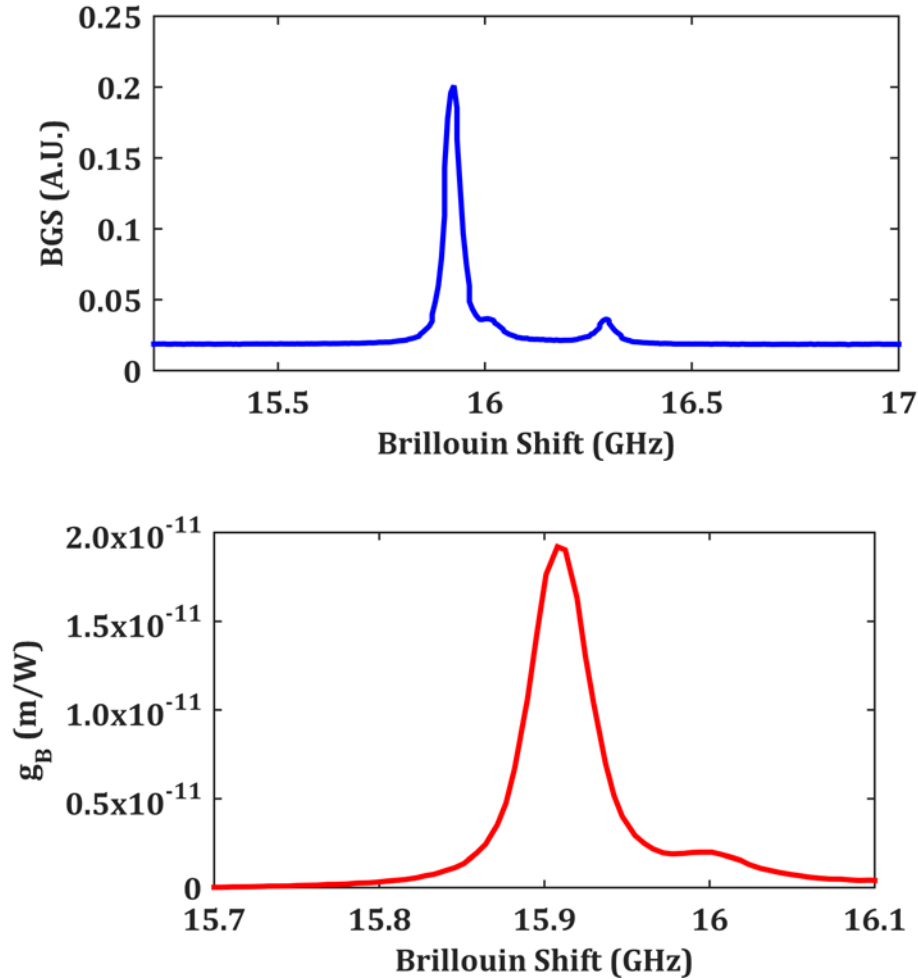


Figure 14: The experimental BGS, scaled to the estimated g_B is shown above for the hybrid fiber. Also shown is a long-range scan revealing a peak due to the pure-silica annulus (top).

The measurement was affected by ytterbium gain saturation. At high pump powers, the pump would saturate the gain and effectively create a lossless waveguide for the counter-propagating probe. This affected the analysis because the 2x2 model assumes a constant attenuation coefficient and in a gain-saturated amplifier the loss coefficient varies with length. Only at pump powers < 6 W was the gain saturation of minimal consequence to affect the analysis. The effects of gain saturation can be seen in figure 15 that shows the observed BG coefficient versus pump power. When high powers are used to pump the fiber, the ytterbium attenuation of the lower-power probe is decreased and more probe light is transmitted. This effect is incorrectly viewed by the numerical

simulations as owing to an enhanced Brillouin gain rather than a reduced, spatially-varying attenuation coefficient.

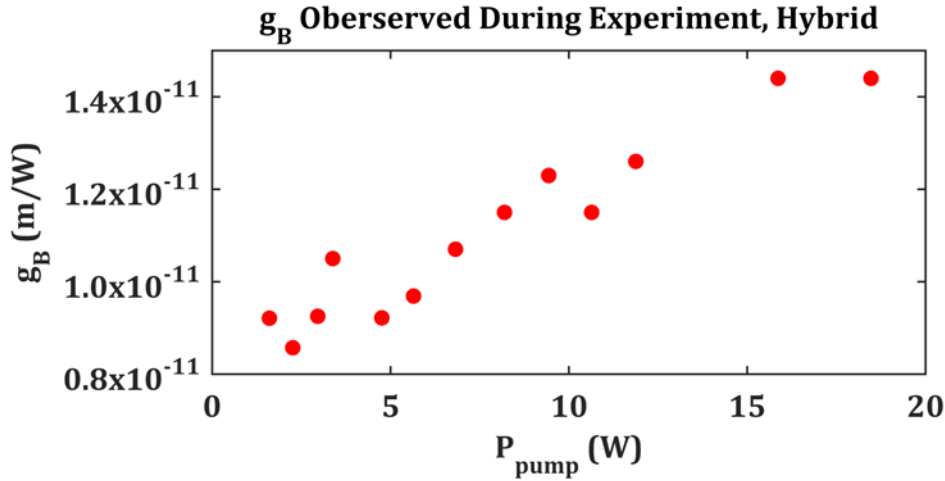


Figure 15: The g_B that best matched simulated and experimental data at each pump power tested is shown above for the hybrid fiber.

Gain saturation was not observed in the interrogation of the PBGF because the phosphate-doped glass engendered higher levels of ytterbium doping [11]. The higher ytterbium concentrations along with the lower intensity engendered by the 50 μm cores makes the saturation intensity much higher in the PBGF.

4.1.7 Theoretical Examination of SBS in Microstructured Fibers

In response to the unusually low g_B from the PBGF found in the pump probe, a numerical model was used to study g_B to validate results. For perspective, the g_B for the silica response in the fiber core was $>7\times$ reduced compare to bulk silica [7] and the g_B for the Yb- and P_2O_5 -doped silica was $4.3\times$ reduced [12] compared to literature values. A $2\times$ reduction can be explained for each response considering that the core is roughly comprised of 50% of each material; thereby lowering the overall response by $1/2$. The remaining reduction in g_B is explained below after the model is introduced.

A. Mathematical Description of Acoustic & Optical Coupling in Fiber

To describe the acoustic-optical wave coupling in fiber, a numerical scheme has been developed to accomplish calculations of g_B without simulating acoustic waveguide properties of the fiber [13]. Also of importance is that this model utilizes first-principles physics of the acoustic and optical properties of the glass waveguide. In this scheme, a non-homogenous Helmholtz formalism with the electric field driving the acoustic displacement is used to describe SBS gain. The wave equations describing optical and acoustic propagation are given as:

$$\frac{d}{dz}a_s(z) = \frac{1}{4}a_p\left(\frac{\gamma}{\epsilon_0}\right)\left(\frac{2\pi}{\lambda}\right)^2 \frac{\langle f(x,y)|\varphi(x,y)|f(x,y)\rangle}{\langle f(x,y)|f(x,y)\rangle} \quad (13)$$

$$\left[\nabla_t^2 + \left(\frac{\Omega}{V_t}\right)^2 - \beta^2\left(\frac{V_l}{V_t}\right)^2 - i\frac{\Gamma\Omega}{V_t^2}\right]\varphi(x,y) = i\frac{2\pi n\gamma}{\lambda\rho V_t^2}a_p a_s(z)f(x,y)^2 \quad (14)$$

where for the optical wave equation, $a_{p/s}$ is the z -dependent electric field amplitude that grows/shrinks along the fiber, f is the transverse guided optical mode intensity profile, γ is the electrostrictive coefficient, ϵ_0 is the permittivity of free-space, and $\varphi(x,y)$ is the acoustic field displacement. Angle brackets indicate an integral over the fiber cross-section. This representation is in the undepleted pump limit. For the acoustic wave equation, Ω is the Brillouin frequency shift (1/s), $V_{l/l}$ is the wave velocity in the transverse/longitudinal direction, β is the acoustic propagation constant, Γ is the phonon decay constant (rad/s), n is the optical refractive index, and ρ is the material density.

Equation (14) reduces to a Greens function, expressed as:

$$[\nabla_t^2 - \kappa^2]\varphi(x, y) = \Phi(x, y) \quad (15)$$

Where:

$$\kappa^2 = -\left(\frac{\Omega}{V_t}\right)^2 + \beta^2 \left(\frac{V_l}{V_t}\right)^2 + i \frac{\Gamma \Omega}{V_t^2} \quad (16)$$

$$\Phi(x, y) = i \frac{2\pi n \gamma}{\lambda \rho V_t^2} a_p a_s(z) f(x, y)^2 \quad (17)$$

and the acoustic displacement can be expressed in integral form as a convolution with a Green's function, given as

$$\varphi(x, y) = \iint G(x, y, x', y') \Phi(x, y, x', y') dx' dy' \equiv (G(x, y) * \Phi(x, y)) \quad (18)$$

The Stokes power and pump power can be expressed as

$$P_{s,p}(z) = \frac{c \varepsilon_0 n}{2} \langle f(x, y) | f(x, y) \rangle |a_{s,p}(z)|^2 \quad (19)$$

The evolution of the Stokes light in the absence of attenuation then yields

$$-\frac{d}{dz} P_s(z) = \frac{g_B}{A_{eff}} P_s(z) P_p \quad (20)$$

With the Stokes gain calculated as

$$\frac{g_B}{A_{eff}} = \left(\frac{1}{\rho c}\right) \left(\frac{\gamma}{\varepsilon_0}\right)^2 \left(\frac{2\pi}{\lambda}\right)^3 \frac{\langle f(x, y) | G(x, y) * g(x, y) | f(x, y) \rangle}{\langle f(x, y) | f(x, y) \rangle} \quad (21)$$

$$g(x, y) = \frac{f(x, y)^2}{V_t(x, y)^2} \quad (22)$$

and

$$A_{eff} = \frac{\langle f(x, y) | f(x, y) \rangle}{\langle f(x, y) | f(x, y)^2 | f(x, y) \rangle} \quad (23)$$

Since these equations become intractable for simple optical and acoustic refractive index profiles for conventional fiber waveguides, a finite element solver has been developed to model the interaction [13]. Leaving the governing equations in the

formalism above assumes no guided wave nature of the longitudinal acoustic wave. Thus, arbitrary acoustic velocity profiles can be simulated for an optical waveguide.

The model estimating g_B is a steady-state solver, meaning no beam propagation is employed. The optical mode is solved utilizing finite element methods developed with Perfectly-Matched Layer techniques [14]. The meshing scheme is curvilinear hybrid edge/nodal element patterning with triangular face shapes [15].

B. Numerical Model of Clemson PBGF

Two CAD designs were used to model the waveguide material arrangement, and are shown in figure 16. The models are color-coded according to acoustic velocity, with a scale shown on the right of each model in m/s. Dark blue is the P_2O_5 - and Yb- co-doped silica. Yellow is pure silica. The cyan is the GeO_2 -doped cladding structures. The change in the two models was in the inclusion or exclusion of sub-optical-wavelength micro-core features. The CAD drawing shown on the left excludes the subwavelength micro-core features and models the actively-doped region of the core as a continuous hexagonal feature that is nearly optically matched to the background silica so as to not engender guiding through total internal reflection (TIR). The second design shown on the right more accurately models the distribution of actively doped regions within the core. The discrete, subwavelength micro-core features are modeled as cylinders with 850 nm diameters distributed within a hexagonal perimeter.

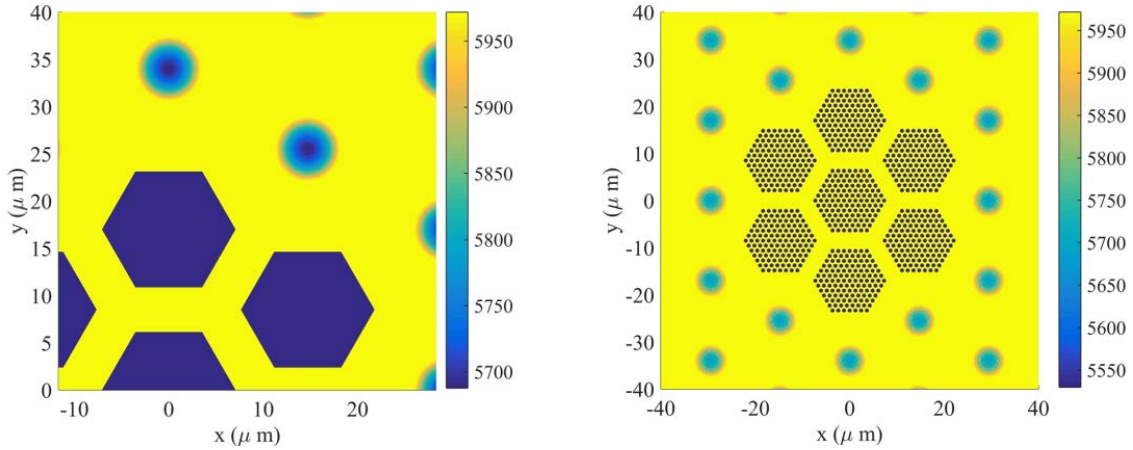


Figure 16: CAD designs for the core of the PBGF. The left design was with coarse core sub-segmentation and the right employs core sub-segmentation with Yb-active regions that are 850 nm in diameter within a hexagonal shell.

Results of the numerical model are shown in figure 17 with the coarsely segmented core on the left and the core including micro-cores shown on the right. The coarsely segmented core shows that the peak g_B interaction is dominated by the pure silica response at 16.3 GHz, and that the magnitude of 0.9×10^{-11} m/W does not corroborate with the g_B estimated from the experimental pump probe. The SBS response of the coarsely segmented core can be explained by the dilution of the core into two discrete materials that are split nearly equally. The finely segmented core, however, produces a BGS that matches very closely with the experimentally estimated g_B . The peak g_B responses of the Yb-active and pure silica regions are nearly equivalent in magnitude.

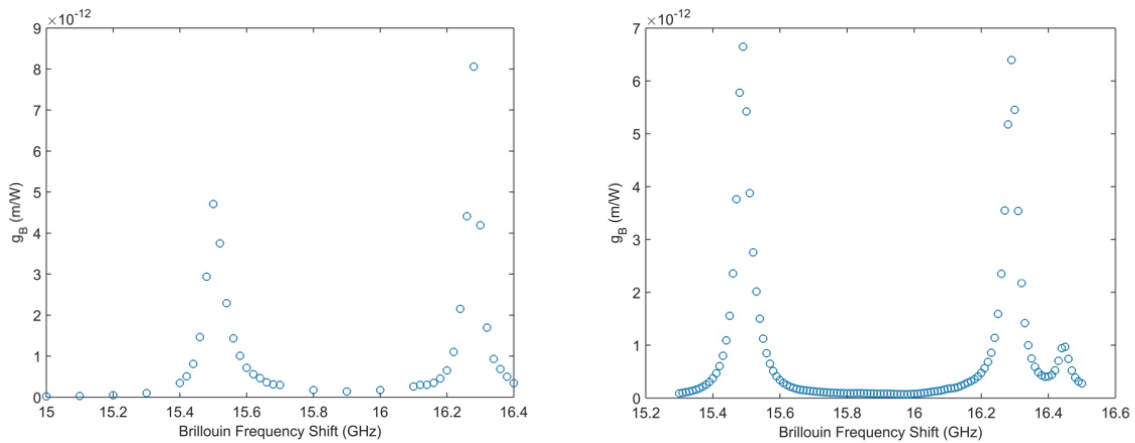


Figure 17: Simulated BG spectra of the coarsely segmented (left) and finely segmented PBGF models are shown above.

It should be emphasized that the CAD drawing that included the subwavelength micro-cores designated more of the core area to pure silica. Yet, the peak SiO_2 g_B response decreased by $\sim 30\%$ in this model when it was expected to increase. It should also be emphasized that no advanced materials with ultra-low acoustic coupling are being modeled. When the finite element solver models a homogenous step-index core, the simulated g_B is 2.4×10^{-11} m/W; which is on-par with Yb-doped step-index fiber. The micro-cores, therefore, must be affecting the dispersion of acoustic energy. Acoustic energy dispersion is accurately modeled with the finite element solver employed because no guided acoustic wave physics is assumed into the model. Acoustic displacement field density at each frequency are simulated, and the results are shown in figure 18. The acoustic displacements due to the Yb-active regions are shown to the left and the pure silica acoustic field to the right.

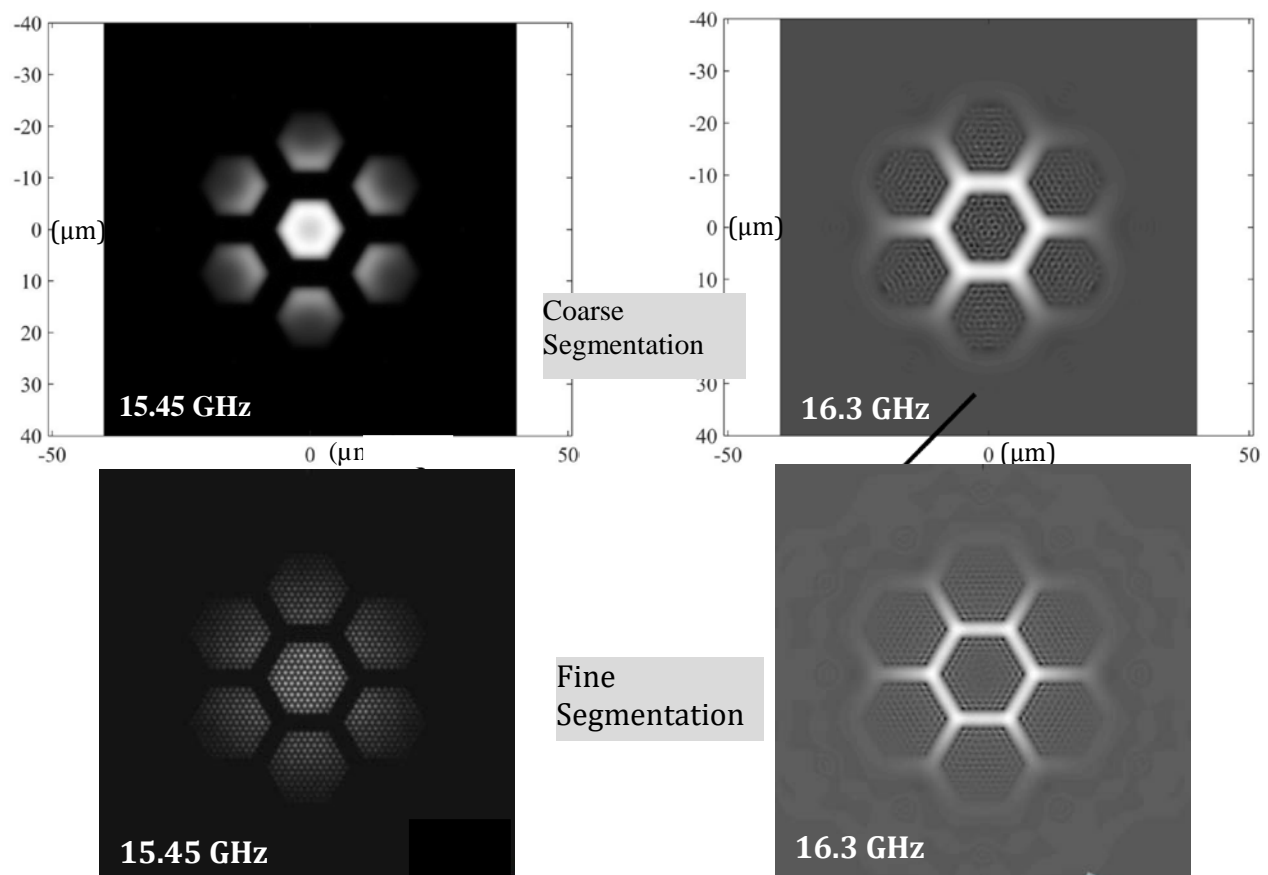


Figure 18: Simulated acoustic displacements showing the acoustic energy density at each Brillouin frequency response is shown above. Responses at 16.3 GHz are pure silica and responses at 15.45 GHz are Yb-active regions.

4.2 Power Scaling Microstructured Fiber Amplifiers

In this chapter, the microstructured fiber amplification limits for both the NKT hybrid and Clemson PBGF are tested in a counter-pumped amplifier configuration. The primary limitation to diffraction-limited, narrow linewidth amplification of these microstructured fibers was the onset of modal instabilities (MI). The first section is devoted to understanding the physics responsible for MI. The second section describes the counter-pumped amplifier configuration along with the suite of diagnostics used to monitor the fiber under amplification. The demonstration of each microstructured fiber is then described in the following two sections. Finally, a discussion at the end of the chapter compares hybrid fiber amplifiers with PBGF amplifiers.

4.2.1. MI Theory

A. Physical Description & Modeling Schemes

Critical to understanding MI is knowing the physical manifestation of the mode coupling in multimode waveguides. Under the current understanding of MI, a coupling mechanism is proposed whereby the longitudinal refractive index profile is modified periodically along the fiber on a length-scale order of the beat length between propagating modes of $L_B = c / [u(N_{eff,i} - N_{eff,j})]$. Here u is the optical frequency and $N_{eff,i/j}$ is the effective refractive index of the i/j propagating modes determined by solving for the eigenmodes of the waveguide [16, 17]. For a 1 μm wavelength and a difference in N_{eff} of 0.0001, this beat length is 1 cm. This interference phenomena is based on experimental observations in LMA rod amplifiers in [18], and the image is reproduced in figure 19. The green photoluminescence from nonlinear optical transitions in ytterbium is modified because wave interference reduces optical amplification at the nodes and the ytterbium emits a stronger spontaneous emission signal instead.

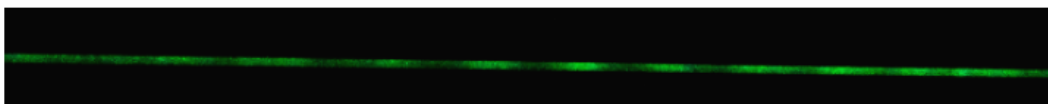


Figure 19: Longitudinal optical interference pattern in LMA PCF whose origin is conjectured as modal interference shown as bright and dark sites for Yb-photoluminescence. The rod is 15 cm long with a 100 μm core diameter.

In an amplifier, this interference pattern reduces optical activity, and the corresponding quantum defect heating, at the interference nodes. This establishes a longitudinal periodic thermal gradient on a length scale of the mode beat length. When the periodic thermal gradient is in phase with the optical mode interference pattern, no coupling occurs. When the dynamics of optical amplification causes the optical field intensity pattern to lead the thermal pattern in phase, dynamic coupling can occur. The loss in phase relation between longitudinal optical and thermal interference patterns is shown in figure 20 based on modeling from [19]. In the figure, the blue optical field interference pattern is initially in phase with the red periodic temperature profile but becomes out-of-phase at high field intensities.

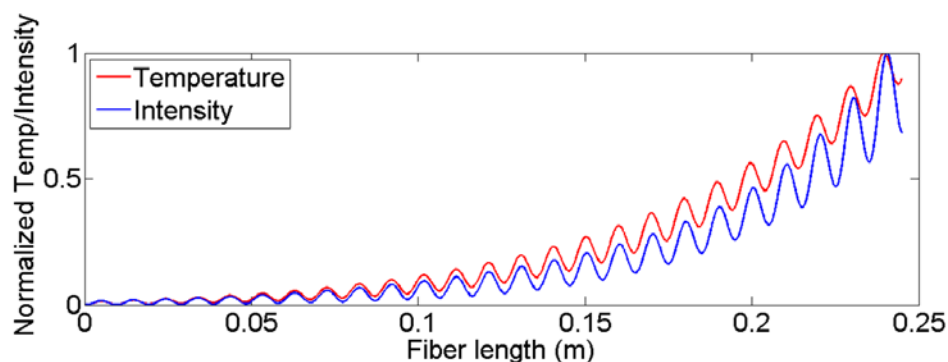


Figure 20: Simulated longitudinal thermal and optical intensity gratings are shown above from a study in [20]. The loss of phase relation between red and blue gratings at high optical intensity is responsible for mode coupling in MI.

Jauregui *et al*/ modeled the coupling with a 3D beam propagation model (BPM) that interrogated the role of a spatially resolved optical gain coupled to the modal interference grating [17]. The longitudinal refractive index gradient is modeled as owing to gain-guiding and anti-guiding, or the so-called Kramers-Kronig effect, whereby the refractive index changes in response to high population inversion of the ytterbium ions. The model accurately predicts an oscillatory coupling between fundamental and higher-

order modes without loss of overall energy. As argued in Smith *et al* [16], however, a second condition necessary for coherent transfer of energy is to include a phase delay between the longitudinal temperature gradient and the modal interference grating. This breaks the symmetry between forward and backward propagation; which is key because experimentally neither forward-propagating mode is observed to couple strongly to the Rayleigh light and should according to the Jena model. The backward wave was not accurately accounted for in the Jena group BPM because the model utilizes the so-called one-way wave equation that only propagates the forward wave.

With the phase dynamics between the temperature gradient and modal interference accounted for in the model, Smith was able to demonstrate that the longitudinal refractive index dynamics was thermal at its origin and is only mildly affected by Kramers-Kronig dynamics, and the authors were able to predict small-signal gain coefficients for the mode coupling process. Attempts by the authors to model the effect without the phase delay resulted in no mode coupling. The model, however, prescribes an artificial phase matching of the two interfering optical modes necessary for coherent energy transfer without positing a mechanism. Furthermore, only the small-signal gain for the mode coupling was analyzed. No temporal dynamics were studied so the model was not able to demonstrate the re-coupling of the higher-order mode to the fundamental mode as is observed in MI.

Ward *et al* [36] developed a time-dependent model that demonstrated dynamic coupling between the modes beyond MI threshold. In addition, a source for the phase matching was posited as a nonlinear phase shift from self-phase modulation in the fiber with additional contributions coming from how the temporal response of the heat and laser gain modifies optical path length. In this paper, the laser gain and temperature rate equations were assumed as steady-state, and no measurables were provided as to the magnitude of the expected frequency difference between propagating modes.

In building off of Ward's work, Naderi *et al* were able to model the mode coupling without directly ascribing a source for the phase lag between the signal intensity and longitudinal temperature grating [89]. The phase delay in this work was physically manifested in the interdependent heat and laser gain equations whereby the temperature and optical fields are influenced by the upper-state population density, N_2 .

N_2 is an independent variable for the optical field equations but is a dependent variable in the heat equations because these must change in response to the field equations. This causes the electric field intensity to lead the thermal dynamics in phase. With this treatment, the observed frequency difference was recovered from a first-principles model and accurate MI thresholds were predicted for conventional step-index fiber and gain tailored photonic crystal fiber (PCF) designs.

B. Role of Photodarkening

As mentioned in chapter 1, one MI mitigation technique is to reduce quantum defect heating by amplifying a signal in a ytterbium-doped amplifier closer to the pump wavelength of 976 nm. Also mentioned was the conditions that would make this a difficult experiment to perform because the seed power influences both MI threshold and ASE dynamics. This experiment was performed by the Jena group in a study that conjectured that the role of photodarkening was very impactful for determining MI threshold [21]. The main experimental evidence from Otto *et al* that photodarkening influences MI threshold is given in a plot in figure 21. The figure shows actual MI thresholds in a 62 μm core PCF according to first observed onset (blue) and several trials after (black) according to wavelength. Recall from chapter 1 that one of the signatures of MI is a hysteresis effect that causes the MI threshold to reduce with each power scaling trial. Also shown is the numerically-derived population inversion according to wavelength in green. The figure demonstrates an optimum MI threshold at 1030 nm wavelengths, and MI threshold is reduced when blue- and red-shifted from 1030 nm. According to relevant MI theory the MI threshold would continuously increase when the wavelength is blue-shifted due to reduced quantum defect heating. Problems exist, however, when analyzing the experiment to determine if the researchers properly seeded the amplifier to mitigate ASE; which can interfere with the modal interference because the ASE optical phase is random and would therefore reduce visibility of the interfering modes. To properly seed the fiber amplifier to mitigate ASE, the seed power must be several orders larger than the saturation power, given below as:

$$P_{sat} = \frac{A_{core} h \nu}{(\sigma_e + \sigma_a) \tau} \quad (24)$$

where A_{core} is the area of the core, ν is the optical frequency, h is Planck's constant, $\sigma_{e/a}$ are the emission and absorption cross-sections, and τ is the upper-state lifetime for ytterbium. With appropriate values in ytterbium at 1030 nm [22], the saturation power for the 62 μm diameter Jena fiber is estimated as 0.81 W. An adequate figure of merit to properly seed an amplifier is to exceed the saturation power by $>100\times$. Naderi *et al* seeded a 20/400 μm core/clad fiber amplifier operating at 1034 nm with 20 W [23] when studying MI at wavelengths short than 1064 nm. This represents a 235x scaling of the seed power relative to the saturation power of a 20/400 μm fiber of 0.084 W. The Jena group, in contrast, exceeds the saturation power only by 25x at 1030 nm with the 62 μm core rod-type amplifier. Saturation powers at 1010 nm and 1060 nm are higher than 1030 nm for the Jena fiber, and are, respectively, 1.12 W and 2.45 W. In the study by Otto *et al*, the seed power was kept constant. At 1010 nm and 1060 nm, the 20 W seed is only 17x and 8x above the saturation power, respectively. The seed power was necessarily kept constant because MI has shown an increased threshold with increased seed power. From the figure, MI threshold is reduced at 1010 nm and 1060 nm relative to 1030. These results suggest that the effect measured was an artifact of an improperly seeded amplifier. From this work, it is difficult to conclude that photodarkening is a major factor in MI threshold physics. But nevertheless photodarkening may play a role in determining MI threshold. A less ambiguous test that the researchers could have attempted was to power scale at wavelengths 1080 nm to ~ 1150 nm to interrogate wavelength dependence on MI threshold. In this spectral domain, the absorption is nearly zero and the emission is much lower but is also nearly constant so a constant seed power would not noticeably affect MI threshold.

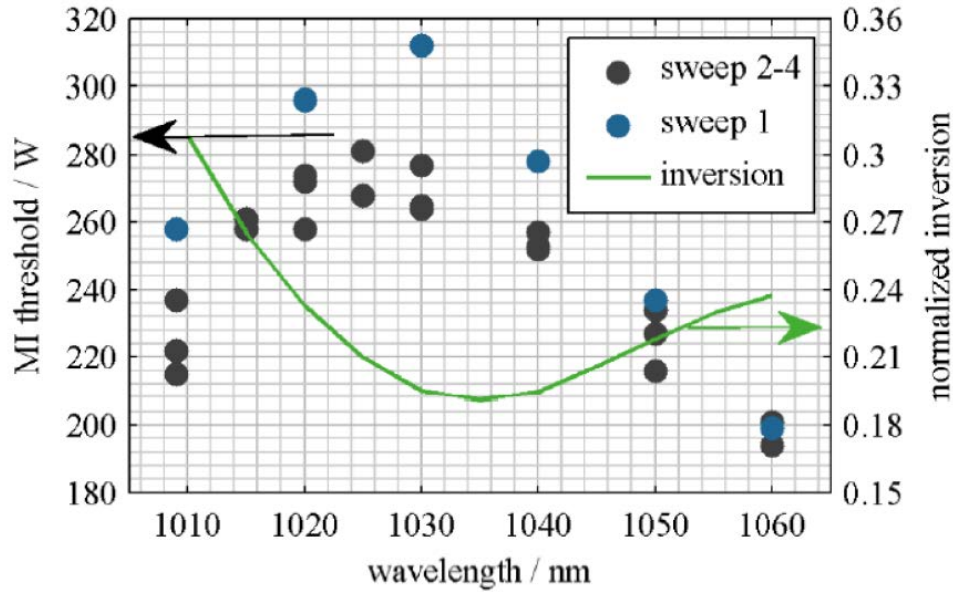


Figure 21: The wavelength dependence of MI threshold is shown above from a study in [21] along with the estimated population inversion curve (green).

There are two types of ASE, and only one is mitigated through proper seeding. The process in which the laser is absorbed and re-emitted spontaneously at the same wavelength, but out-of-phase with the original field can be mitigated by seeding at higher powers and thereby saturating the gain at the laser wavelength. The process in which the laser signal is absorbed and re-emitted at longer wavelengths is unavoidable unless spectral filtering fibers are utilized.

C. MI in Raman Fiber Amplifiers

A less ambiguous test than Otto *et al* to determine the role of photodarkening in MI dynamics may come in the form of power scaling LMA, cladding-pumped Raman fiber amplifiers (CPRFAs). CPRFAs provide an interesting platform to experiment with MI because of an absence of rare-earth dopants that are the cause for photodarkening. Core pumped raman fiber amplifiers (RFAs) are not a good choice to test this effect because the brightness of core pumped RFAs are limited by the pump source. The major discrepancy between MI dynamics in CPRFAs and Ytterbium Doped Fiber Amplifiers (YDFAs) that clouds an exact comparison for testing photodarkening is that the Raman amplification along the length of a fiber is highly nonlinear, and leaves much

of the amplification, and corresponding quantum defect heating, at one of the boundaries. Physical models have been proposed on MI in CPRFAs [24], and validate that MI behaves differently. Notably, gain-tailoring of the core in CPRFAs does not offer a significant increase in MI threshold.

4.2.2 Counter-pumped Amplifier

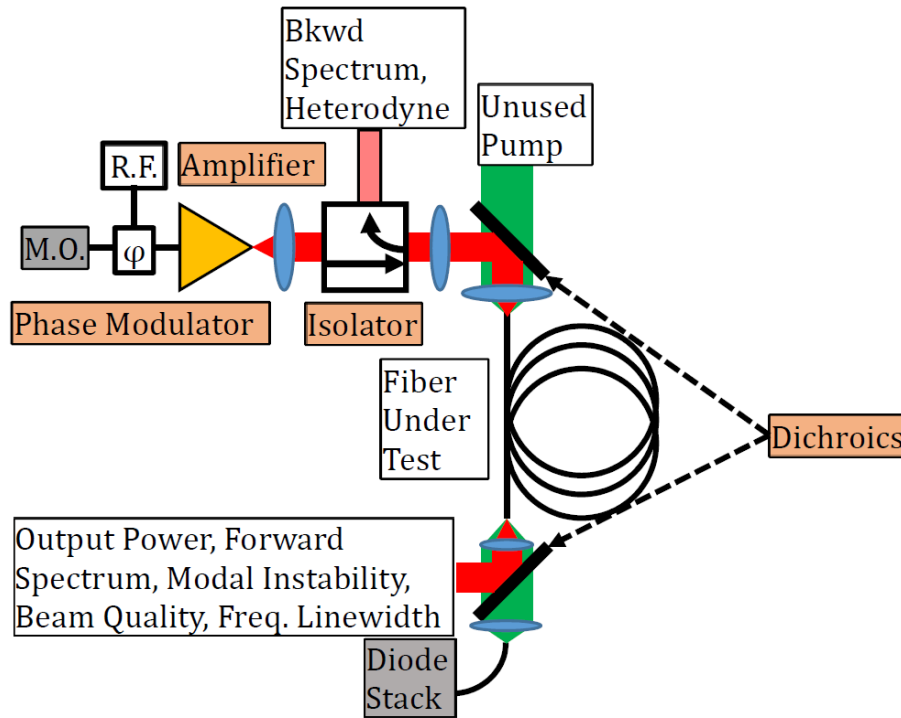


Figure 22: A schematic of the counter-pumped amplifier is shown above.

The free-space counter-pumped amplifier system is shown as a schematic in figure 22. A 1064 nm non-planar ring oscillator (NPRO) with a nominal frequency linewidth > 10 kHz is amplified in a 3-stage ytterbium-doped fiber amplifier from IPG photonics. The ~ 35 W output has PER > 20 dB, $M^2 < 1.2$, negligible ASE and is functional with single-frequency or phase-broadened seeds. A free-space Faraday isolator from EOTech is used to collect backward-propagating light for spectral analysis. A 2-lens system is used to mode-match the seed beam waist at focus with the waveguide mode. An optimum design is initially posited using a wave optics simulation of the propagating beam with ABCD matrices representing the lenses to properly prepare a beam waist of the desired

width to match the fundamental optical mode of the fiber. This design is then optimized in practice by fine-tuning the distance between the two lenses to optimize the transmitted beam M^2 at the fiber output.

A fiber-coupled magnesium-doped lithium niobate phase modulator from EOSpace is utilized for phase broadening, if needed. Phase broadening of the signal occurred before amplification in the IPG amplifier. The 1.3 kW 976 nm fiber-coupled diode stack from Laserline is coupled into the inner cladding waveguide of the double-clad fiber. Dichroics are used to separate the pump and signal beams inside an enclosed housing that is actively water-cooled; which is necessary because stray pump light from the multimode pump fiber will heat the metal clamps holding the mirror and will cause unwanted thermally-induced beam steering if left uncooled.

Unless otherwise noted, fiber facets are prepared by stripping the polymer coating and angle-cleaved to $\sim 4^\circ$ to prevent parasitic laser oscillations engendered by Fresnel reflections from competing with amplifier gain. The fiber tips are placed in aluminum chucks that are actively water-cooled and sit atop 5-axis stages that are necessary to align the beam due to the angle-cleave. Fibers are spooled, with attention paid to maintain a constant coil axis, on aluminum spools. Arriving at the optimum diameter for coiling of each fiber will be detailed below. Maintaining a constant bend axis relative to the photonic structure of the microstructured fiber was critical to accurately study MI.

The suite of diagnostics used to characterize amplifier performance includes: power meters to measure amplified signal and unused pump power, optical spectrum analyzers (OSAs) to characterize the forward and backward spectra from the amplifier, a spatial mode scanning M^2 beam quality analysis system, a high-speed camera to capture the onset of MI, and a self-heterodyne frequency analyzer. The last diagnostic is used to capture high-resolution BGS of the spontaneously-generated Stokes light in the amplifier *in-situ* while the amplifier is active so that comparisons can be made with the pump probe. In this setup, a sample of the NPRO is mixed with the backward-propagating light in a 3 dB splitter and the mixed signal illuminated a fast (26 GHz 3 dB bandwidth) photodiode from Newport. The resulting signal, read on a radio frequency spectrum analyzer, is the convolution of the two signals.

The amplifier is susceptible to parasitic pulsing that can damage the fiber due to ASE and/or SBS processes. The initial damage to a small section of the fiber can be exacerbated if the core is damaged and the signal loses guidance. In this case, a large section of fiber will be pumped and unseeded; which will almost certainly result in more extensive pulsing and the fiber can ignite. To prevent this, an electronic shutdown system continuously monitors the output power and will sequentially shut down the signal seed, pre-amps, and the pump if power momentarily drops. The circuitry response is ~60 ms and is limited by mechanical responses of onboard relays. Ideally, however, circuit response would be closer to the ~1 ms time scale for ytterbium upper-state lifetimes so that significant build-up of inversion can be avoided if the seed is lost.

The counter-pumped scheme has advantages for free-space-coupled amplifiers over co-pumped architectures for both performance and optical design reasons; which are detailed below. From a seed coupling perspective, the compatible optical systems for a co-pumped amplifier are very restrictive because both the signal and pump beams must have coincident foci while the signal beam profile must match the fundamental mode profile to properly seed the waveguide. This becomes cumbersome because the low-brightness pump light restricts the number of short focal length (< 100 mm) lenses that can be used while coupling the seed to the core is more manageable with more lenses. The design is exacerbated with the additional complexity of correcting for beams that are not collinear; which can occur if the multimode fiber containing the fiber light is not precisely collimated. Additional beam steering methods must be used to steer the seed or pump while introducing minimal aberrations because a 5-axis stage can only be aligned to the seed or pump.

The counter-pumped amplifier, in contrast, does not rely on each beam having coincident foci. The seed beam can utilize the requisite number of optics to efficiently couple to the waveguide core without necessarily considering the effects of the pump, and vice versa. Each beam can also be steered independently so as to ensure each beam passes through critical optics in the center to minimize aberrations, and the 5-axis stage used to mount the fiber can be aligned to the respective incoming beam.

The laser gain along the fiber depends on pumping direction as well, as was shown in figure 2 in section 3.1. In a counter-pumped configuration, the highest ytterbium

inversion levels are coincident with the highest signal optical fields and overall power levels along the fiber are not high until the end of the fiber. This contributes to a favorable SBS threshold compared to co-pumping as described in section 3.1.

4.2.3 Hybrid Microstructured Fiber Power Scaling

A. Linewidth Broadening Schemes Employed

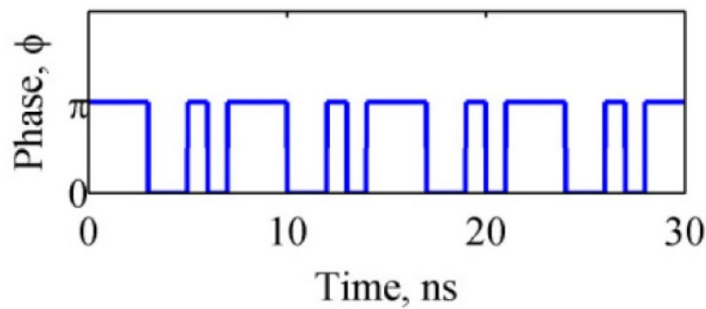


Figure 23: A temporal response of the optical phase modulation sequence for a 1 GHz clock rate, 7 bit pattern PRBS scheme is shown [25].

The Pump Probe BGS experiments with this fiber, described in section 3.1, indicated that the natural BG coefficient was too high for single-frequency power scaling. Phase broadening by applying a pseudo-random bit sequence (PRBS) bit pattern to an electro-optic phase modulator was employed to mitigate SBS. In PRBS phase broadening, a modulation depth between, say, zero phase shift and the π phase shift is determined. The voltage difference between the zero phase shift voltage and the π phase shift voltage on the electro-optics modulator, herein referred to as V_{π} , is then discretized by an integer number of bits and the PRBS sequence modulates between those discrete drive voltages on time scales shorter than the phonon lifetime. The resulting temporal response of the phase is rectangular pulses with varying temporal widths, and is shown schematically in figure 23. The Fourier transform of this pattern is a sinc^2 envelope, with a bandwidth of the drive frequency, with discrete tones due to the random sequencing. The number of discrete tones within the sinc^2 envelope depends on the number of bits between 0 and V_{π} . A power spectral distribution of the optical output of a PRBS signal is shown in figure 24. PRBS phase broadening has been shown as superior to white-noise

phase broadening [25], and the advent of low V_π , fiber-coupled Lithium Niobate external phase modulators makes this SBS suppression technique ideal for all-monolithic and free-space fiber amplifiers.

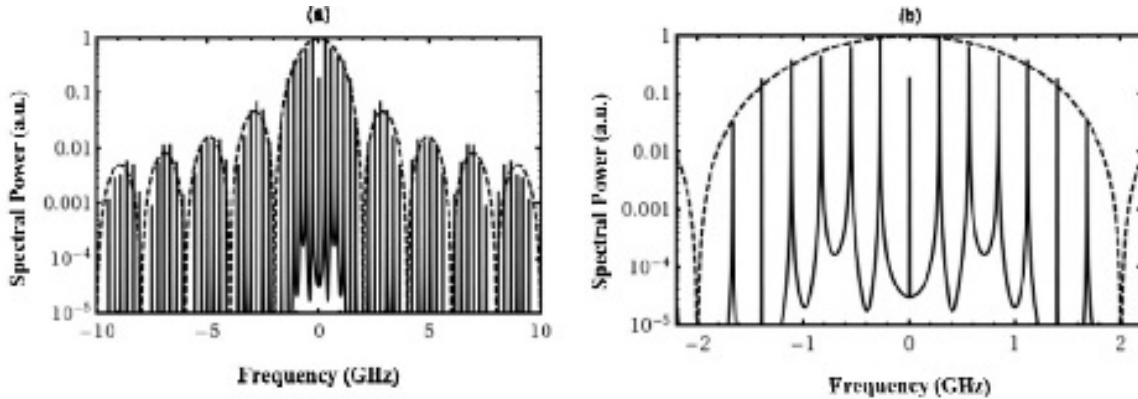


Figure 24: The power spectral density of an optical signal after PRBS phase modulation with a 7 bit pattern driven at a clock rate of 2 GHz is shown above [26]. The left shows a long-range power spectrum while the right shows a more narrow frequency range with emphasis on the discrete tones comprising the total response.

To find the optimal bit sequence and frequency settings, we utilized the figure of merit offered by Zeringue et al [26] in which the spacing between the discrete single-frequency tones underneath the sinc² enveloped are spaced by a multiple of the Brillouin gain bandwidth. In the case of the hybrid fiber, which had a measured BG bandwidth of 42 MHz, a 1 GHz clock rate with a 15 bit sequence was chosen. This provided a spacing between discrete tones of 66 MHz, or nearly 1.5x the BG bandwidth. Optimal suppression for a given clock bandwidth is realized for a spacing between discrete phase modulator tones of 2x the BG bandwidth. The argument for 2x the BG bandwidth being optimized is that the Brillouin response of each discrete tone will not appreciably seed one another while a bountiful amount of tones are available to disperse the spontaneous Brillouin scattering. Our selection approaches this optimized value.

In addition, the PRBS signal electronics were filtered to remove higher-order tones of the sinc² envelope from the power spectral density. This had the effect of drastically reducing additional frequency spectra beyond the primary sinc² envelope. The low pass filter used to filter the RF spectrum was chosen to be 1/2 of the clock rate of the PRBS system. The filtered spectrum can be seen in Figure 25 as detected using a heterodyne

system in which the broadened laser and master oscillator are mixed and illuminate a fast photodiode detector.

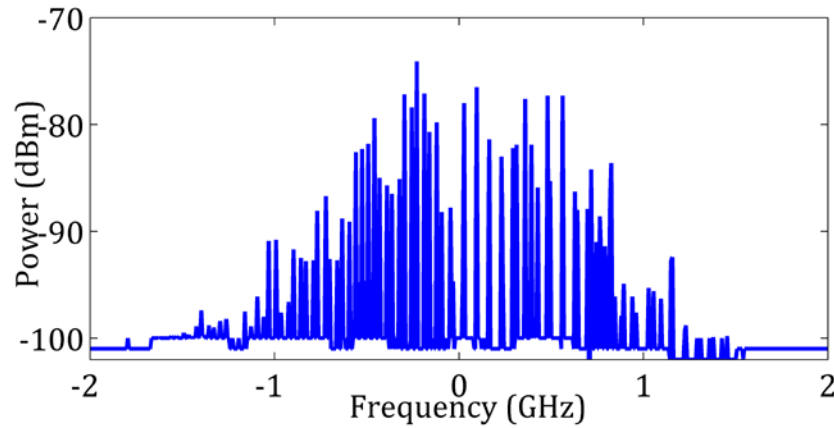


Figure 25: The output spectrum of the seed due to phase broadening is shown above in the hybrid fiber power scaling experiments.

Table 2

Hybrid fiber amplifier test specifications and results – 3 separate fiber draws

	Draw 1	Draw 2	Draw 3
Wavelength	1064 nm	1064 nm	1064 nm
Core/inner cladding diameter	37/370 μm	35/350 μm	35.5/355 μm
Phase Broadening Pattern	Sinusoid	PRBS	PRBS
Linewidth	800 MHz	1 GHz	1 GHz
Sub-MI B.Q.	1.1-1.2	1.1-1.2	1.2
SBS	> Rayleigh	None	None
ASE Depth	> 45 dB	> 45 dB	25 dB
Length	~9 m	~9 m	7.3 m
Coil Diameter	65 cm	65 cm	65 cm

Three hybrid fiber draws were tested. All three were from the same preform, but were drawn with different fiber draw settings; which produced three core/inner cladding diameters: 37/370 μm , 35/350 μm , 35.5/355 μm . Results are summarized in table 2 in which output power, limitation, phase broadening scheme, beam quality, and nonlinear optical responses are listed. The experimentation of each draw will be described below.

Also, the optical-to-optical efficiency, unless otherwise noted, is taken with respect to the launched pump power from the fiber emitting the diode light. The launched pump light will experience ~4% Fresnel reflection at the air/glass interface. Other efficiency metrics for free-space fiber amplifiers that are found in the literature include efficiency with respect to the coupled pump and the absorbed pump. The coupled pump discounts the 4% Fresnel reflections and the absorbed pump discounts the Fresnel reflections and the unused pump as measured on the appropriate power meter. Thus, when referencing optical-to-optical efficiencies in the literature it is important to distinguish which metric is being discussed.

B. 37/370 μm Diameter Fiber

The 9 m amplifier was scaled to 750 W with $M^2 < 1.25$ and frequency bandwidth of 800 MHz before thermal issues caused the fiber to fail. Figure 26 shows the amplified signal versus launched pump for the first draw fiber. Notice the shift in conversion

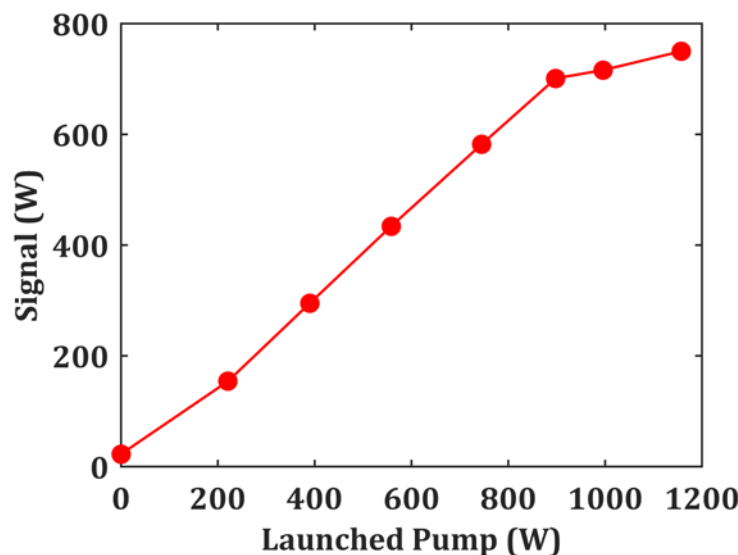


Figure 26: The pump power versus signal power for the 37/370 μm diameter core/clad is shown above. The change in response at 900 W pump is due to parasitic beam steering of the pump.

efficiency at 900 W pump power. This was due to parasitic beam steering engendered by stray pump light heating the dichroic mount. The pump began to couple into the

second cladding; which was in contact with the brass cooling chucks. The heating due to brass absorption caused the fiber to fail.

Before failure due to thermal effects, both MI and SBS demonstrated signs of threshold. The backward OSA high-resolution spectrum at 720 W signal power, shown

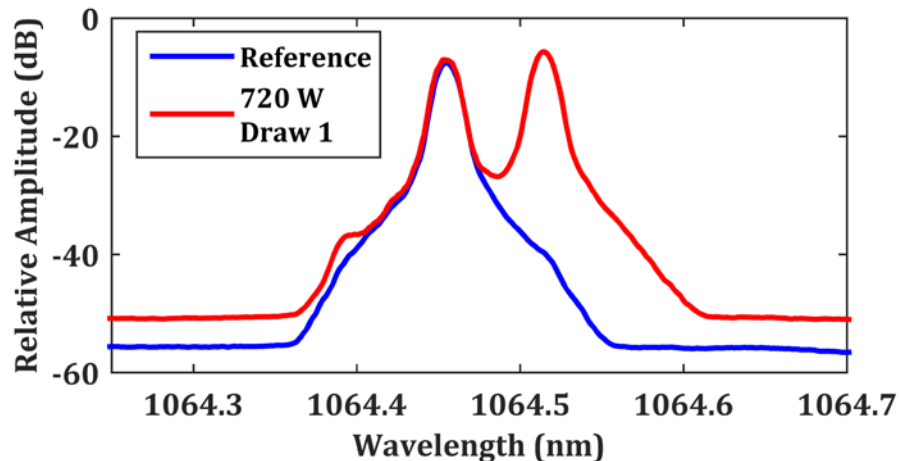


Figure 27: A high-resolution optical spectrum of the backward light is shown above. The spectrum of the 37/370 μm fiber under test is shown with ample Stokes light along with a reference spectrum with no Stokes light.

in figure 27, shows the Rayleigh-scattered component of the spectrum with equal magnitude to the longer-wavelength Stokes-scattered component. Sufficient Stokes light is present in the fiber to cause catastrophic damage when the backward spectrum consists of Stokes light greater than or equal to the Rayleigh light. This is the case in the figure because the Stokes light at ~ 1064.55 nm is nearly equal in magnitude to the Rayleigh light at ~ 1064.45 nm. The phase broadening scheme employed for this experiment was a sinusoid pattern that continuously changed the drive voltage on the phase modulator between $0-V_{\pi}$ at 400 MHz. The high level of Stokes light in the fiber demonstrates that this phase broadening scheme was insufficient for high power. The poor performance of this phase broadening scheme engendered the implementation of the PRBS phase broadening system discussed above.

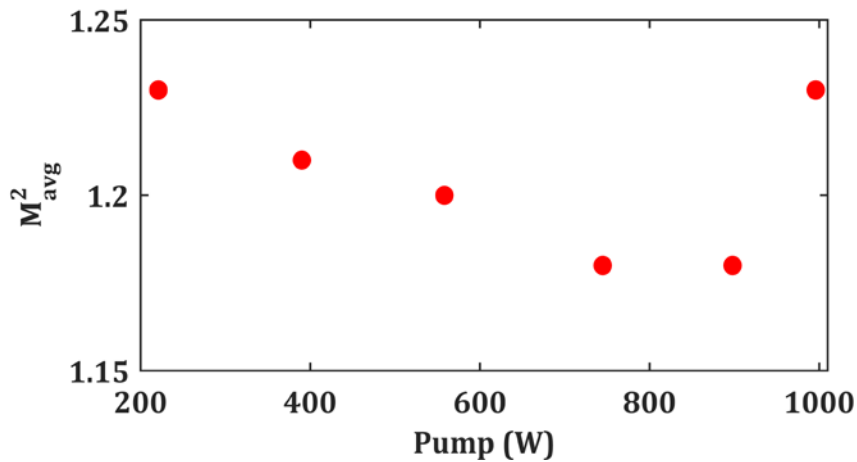


Figure 28: M^2 beam quality versus signal power is shown above. The uptick in M^2 at high powers may be a precursor to MI.

The beam quality also showed signs that MI onset was pending. Figure 28 shows a M^2 versus pump power plot that shows an uptick of M^2 at high pump powers. This, unfortunately, is not an unambiguous sign that the fiber was suffering from MI. The aforementioned beam steering that was affecting the pump coupling was also steering the signal output. This signal output was also used to interrogate the beam quality and was illuminating the Spiricon beam analyzer focusing lens at non-normal incident angles. This introduced aberrations to the beam that could also explain the increase in M^2 .

During subsequent testing, the fiber was fractured while spooling. Neither of the lengths produced after the fracture would have been sufficiently long to produce the high efficiencies needed to compare with standard Yb-doped fibers. Therefore, it is unknown if the more advanced phase broadening schemes applied to the following fibers would have identified the MI threshold unambiguously.

C. 35/350 μm Diameter Fiber

The 9 m amplifier was MI-free up to 820 W with near-diffraction-limited, SBS free output. Figure 29 shows the amplified signal power versus pump power. The amplifier operated at 78% efficiency when considering launched pump power.

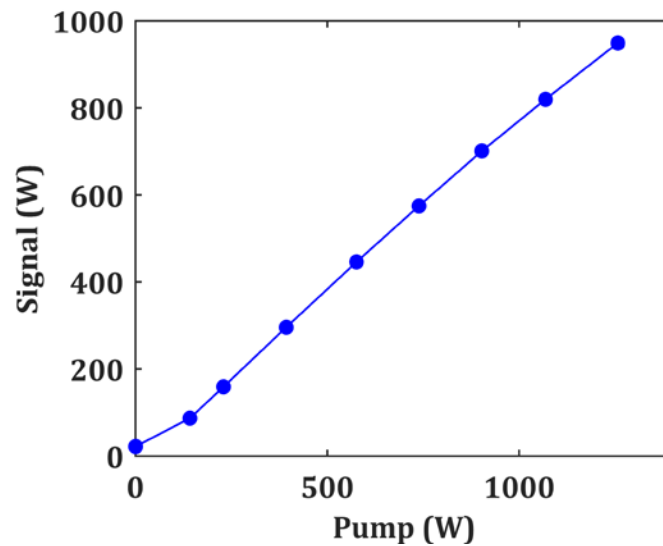


Figure 29: The optical-to-optical power efficiency is shown above along with corresponding M^2 values.

During subsequent measurements, the fiber pulsed ~3 m into the fiber creating two useable sections that were 6 m and 3 m in length, but neither of these was scalable to powers beyond 800 W because pump absorption was too low.

The 1 GHz, 15 bit sequence PRBS phase broadening scheme used to limit SBS was proving effective at these power levels, as no Stokes light was detected in the high-resolution OSA scan. At this frequency separation, trace Stokes light can reliably be measured for depths below the Rayleigh light of ~30 dB. This indicates that the Stokes light was propagating with at least 30 dB less power than the Rayleigh light in the hybrid fiber.

At power levels above 820 W, dynamic MI onset was observed as evidenced dually by a rapid degradation in beam quality and in observation of higher-order mode content appearing in ~0.5 ms periods with the high-speed camera. Figure 30 shows individual frames from the high speed camera. Images were acquired at a frame rate of 20,000 frames/sec. The figure shows rapid coupling of the fundamental mode and the first higher-order mode.

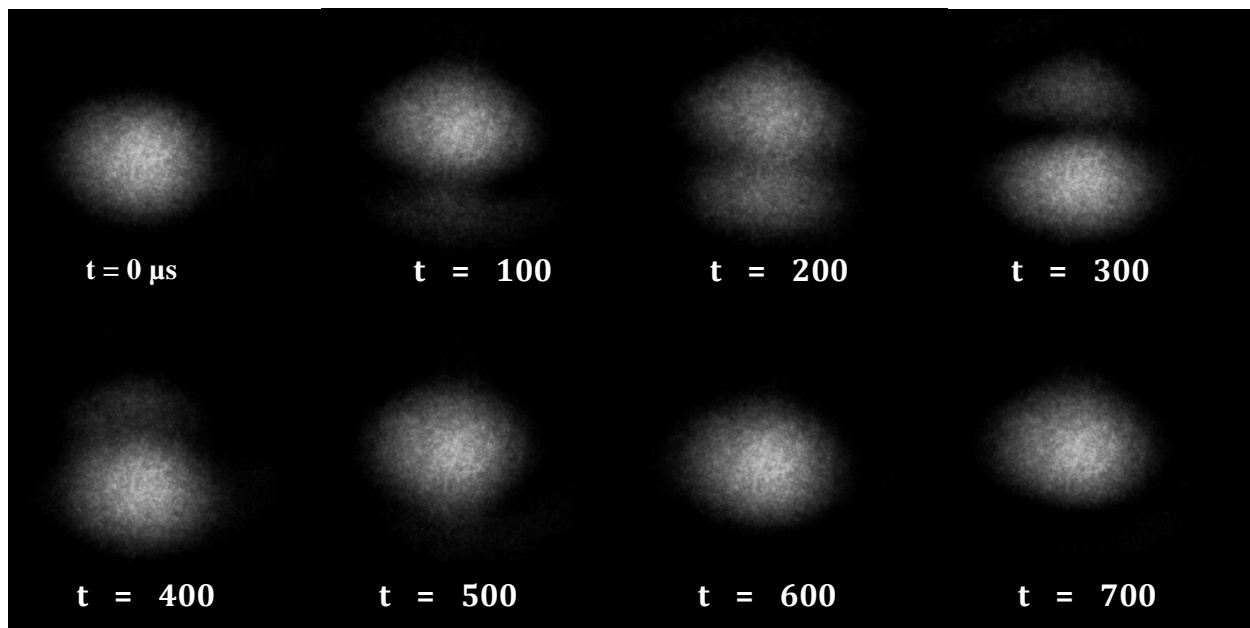


Figure 30: Individual frames from a high-speed camera showing modal instability.

It is interesting to note that MI occurred within the axis defined by the air gaps; which is ostensibly able to more robustly guide the fundamental mode and strip higher-order modes. This is evidenced by analyzing the M^2 of each fiber axis versus pump power as shown in figure 31; which shows the orientation of the high-index and air gap cladding structures as an inset. This, however, does not offer unambiguous evidence that directly tests the MI mitigating tendencies of PBG guidance versus modified-TIR. A fully time-dependent, 3D beam propagation model to study these effects would provide more clarity as to the better guiding mechanism to prevent MI.

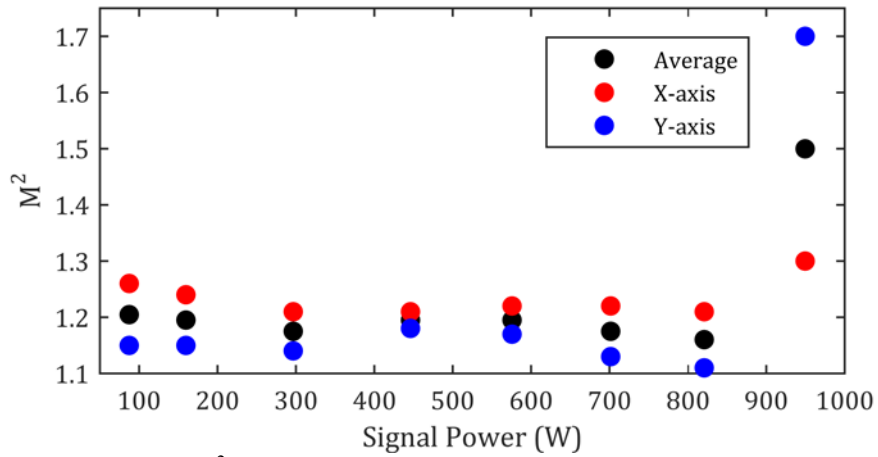


Figure 31: x- and y-axis M^2 values versus pump power showing MI onset occurred in the y-axis; which is guided by air gaps. Inset: the orientation of the high-index and air gap cladding structures.

D. 35.5/355 μm Diameter Fiber

The 7.3 m length of fiber was scaled to 203 W before parasitic pulsing from ASE catastrophically damaged the fiber. The same 1 GHz PRBS phase broadening pattern was employed as in the 35/350 μm core/clad fiber. At these power levels, no evidence of Stokes light was resolved on the backward OSA trace. The M^2 measurements demonstrated near-diffraction-limited propagation of $M^2 < 1.2$.

The cause for the catastrophic pulse was ascribed to ASE as evidenced by the forward OSA trace from 1 μm to 1.13 μm shown in figure 32. The ASE centered at 1040 nm is a mere 25 dB below the signal peak at 1064 nm. Typical ASE suppression is well-performing when the ASE is at a depth of >40 dB below the signal as measured on the OSA. The other two draws measured ASE depth on the forward OSA as > 45 dB at high powers.

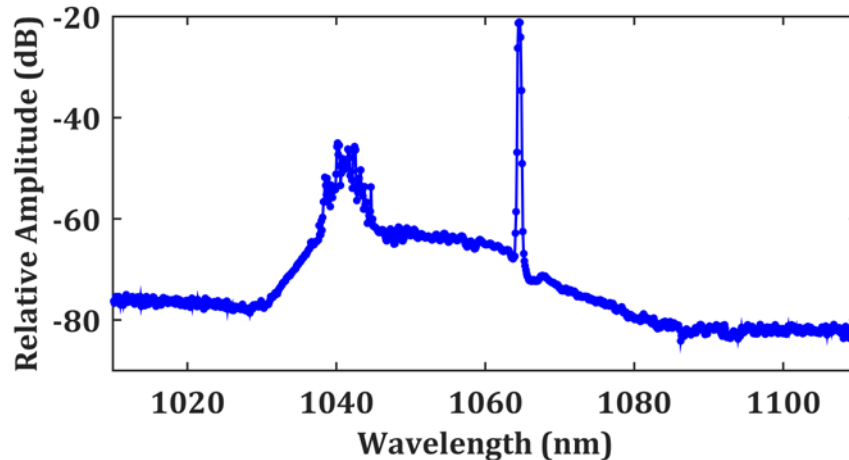


Figure 32: The forward OSA trace of the 35.5/355 μm diameter core/clad fiber design is shown above. The high levels of ASE centered at 1040 nm caused a self-pulse that catastrophically damaged the fiber.

The high levels of ASE are propagating in the fiber because the PBG filter from the high index rods are inadequately filtering wavelengths < 1060 nm. The poorly-placed PBG filter is further evidenced by the poor optical-to-optical efficiency at 1064 nm. The 70% efficiency is inadequate compared to the $\sim 80\%$ efficiencies from the two similar fiber designs. The poor efficiency is caused primarily by the PBG filter attenuating the 1064 nm signal. Optical-to-optical efficiency was also negatively impacted by the shorter length of this fiber. With the observed 1.8 dB/m absorption at 976 nm, the 7.3 m fiber absorbed 13.14 dB of the pump as opposed to the 16.2 dB estimated pump absorption from the 9 m fibers described above. The change in absorbed pump due to length is only 2.5%.

The cause for the inefficient PBG filter is ascribed to the different bending radius of the free-standing fiber loop. With the fiber length provided, each wrap does not fit taut on the coil. A free-standing loop that is larger in diameter than the coil ring is needed to account for the additional fiber length. In the 9 m fiber, this free-standing loop was 75.5 cm in diameter whereas the 7.3 m fiber has a free-standing loop diameter of 86.4 cm. The 86.4 nm diameter is 32% larger than the coil ring. This larger bend diameter deleteriously blue-shifted the PBG transmission spectral band.

E. Discussion

The best performing fiber design was the MI-limited 35/350 μm core/clad fiber. This fiber was also drawn with the smallest core and had the most narrow mode field diameter. That the most MI-resistant fiber tested also has the smallest core diameter is concordant with coupled-mode MI theory because this waveguide is expected to have the largest frequency spacing between propagation constants, and thus the optical mode beating interference will be smallest. This affects MI, in part, because thermal diffusion from the longitudinal thermal grating can interfere with the process and smaller gratings are more strongly influenced by this.

Microstructured fibers are susceptible to mechanisms that reduce efficiency that are not found in conventional step-index fiber. These include: confinement losses to the fundamental mode, pump coupling to the high-index rods, and increased scattering losses in highly-doped GeO_2 rods. Additional reduction in efficiency can be expected due to the gain tailoring employed to mitigate MI because not the entire core is ytterbium-bearing. The observed optical-to-optical efficiency of 78% in the second draw is on par with conventional step-index fibers. This demonstrates that the effects due to microstructures and gain tailoring do not noticeably affect amplifier performance.

Optimization of the PRBS linewidth was not possible because each fiber experienced catastrophic failure during power scaling that caused fiber failure. After each fiber failure, no section of fiber was > 6 m, and power scaling a short section with low Yb concentrations would result in an inefficient MOPA. It is expected that more narrow PRBS patterns will be able to sufficiently suppress SBS.

4.2.4 All-Solid Photonic Bandgap Fiber Power Scaling

The 50 μm diameter core and low g_B of the PBGF were both conducive for high power demonstrations of single-frequency power scaling. As such, no overt linewidth broadening tactics were used. Single-longitudinal mode behavior of the oscillator was verified with a 1 GHz free spectral range Fabry Perot interferometer. The oscillator remained mode-hop-free for 10's of hours while under inspection. In this study, the free-standing loop was kept to a minimum so as to not interfere with the results because the photonic resonance condition in PBGF is dependent on bend diameter. The coil axis of

the fiber in the experiments below was with the flat edge of the photonic lattice of the PBGF parallel to the coil axis. The other extreme for PBGF coiling is for the fiber to be coiled about the intersecting point on the photonic lattice.

A. Replication Study

The first experiment was to duplicate the results published in [27] with a similar coil diameter and the same fiber, but with strict coil control implemented; which is to say that the same flat edge of the hexagonal fiber was touching the spool throughout the full 7.3 m of coiling. The 70 cm diameter coiled amplifier reached single-frequency, MI free amplification up to 368 W; which is 38 W lower than Pulford *et al* achieved. This lower MI threshold is consistent with a hysteresis effect commonly encountered with MI-suffering fibers. The origin of this hysteresis is believed to be a process that writes the modal interference grating into the fiber by ytterbium concentration clustering. This experiment demonstrates, among other things, that strict coil control cannot provide enough differential mode loss to increase MI threshold. In the previous study, the fiber was coiled with multiple 360° rotations of the photonic lattice about the axis of cylindrical symmetry within the 7.3 m fiber.

The launched pump vs amplified signal power is shown in figure 33 for each power scaling sequence. The replication study, in blue, was able to duplicate the optical-to-optical efficiency of 79%. The depth of ASE as measured on the forward OSA was > 45 dB below the signal peak. No Stokes light was observed from the backward OSA in the replication study. The PBGF is similarly susceptible to the reductions in efficiency listed above for the hybrid fiber. The demonstration of a 79% optical-to-optical efficiency demonstrates that these fiber waveguides can be reliably power scaled with high conversion efficiency.

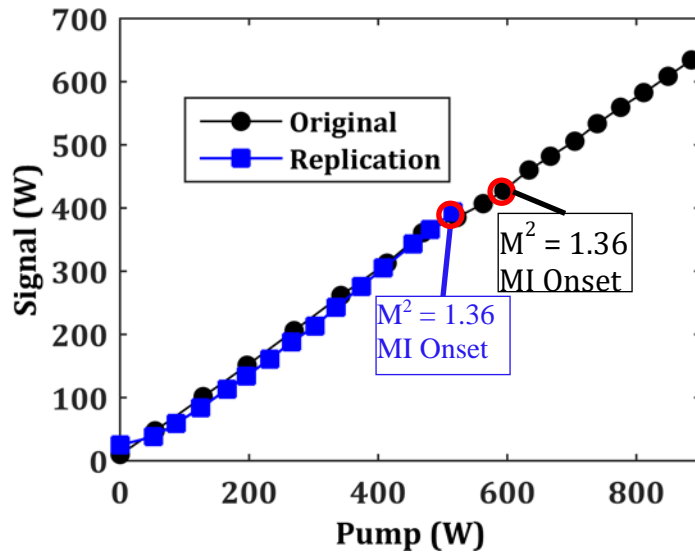


Figure 33: The amplified signal versus launched pump is shown above for the Clemson PBGF. The original power scaling data is shown in black while the replication study is shown in blue. Markers indicate the onset of MI in each case as evidenced by the rapid increase in M^2 .

B. Out-of-Resonance Fiber Power Scaling

The optimization of environmental parameters of the power scaling experiments above was done with low seed and no pump power. The shift in the PBG resonance condition in response to bending, heating, thermal expansion, and gain dynamics that occurs at high powers is not easily simulated, and was not corrected for in the experiments above. The goal of the study discussed below was to power scale a fiber that performed poorly at low powers to determine if the dynamics of the fiber in response to high heat and stress loads shifted the photonic resonance favorably or unfavorably.

The fiber was coiled on a 43 cm diameter ring. At low powers, the $M^2 > 1.35$ was due to high levels of cladding light in the fiber. The mode behavior was stable on the high speed camera; which indicated that the poor beam quality was a steady-state effect and not due to MI. The forward spectrum at low powers was free of any non-seeded signals, so ASE was not to blame for the poor M^2 . The origins of this cladding light is conjectured as being 1064 nm light initially seeded to the core of the waveguide, but that was stripped from the core to the cladding because the PBG waveguide attenuates 1064 nm.

The same section of MI-limited fiber discussed in the original and duplication studies was used for this study, though 1 m removed to minimize the free-standing loop. As is the case with the studies discussed above, no overt linewidth broadening tactics were implemented.

While the coil was actively cooled with forced air, the amplifier was scaled to 347 W; after which MI threshold was achieved. No section of the 6.3 m fiber was observed as being heated above 60 °C. Temperature was monitored with a hand-held thermal camera. The optical-to-optical efficiency was 69%. The reduction in conversion efficiency compared to the 70 cm diameter coil was not significantly affected by the shorter length. Only an estimated 2.5% more pump light was absorbed in the longer fiber. The reduction in efficiency is prescribed to the PBG filter attenuating the 1064nm. Thus, the PBG resonance does not favorably affect power scaling when the bend radius is sub-optimal when no heat or stress gradients due to quantum defect heating exist.

This same fiber was then power scaled in the absence of continuous cooling. Instead, forced air cooling was introduced locally to the sections of the fiber that exceeded 80 °C solely to prevent thermal failure. With this variation, the MI-free threshold was scaled to 388 W; which is 11% higher than when continuously cooled. The fiber amplifier performed similarly poor on the optical-to-optical efficiency at 69% conversion.

When cooling is introduced locally, the majority of the fiber is not sunk to cooling elements and the temperature at the boundaries of the fiber is increased. This favorably affects the MI threshold because the transverse temperature gradient is reduced when the boundaries are not sunk to cooling. This explains the 41 W increase in MI threshold between the continuously-cooled and locally-cooled fiber amplifiers.

4.2.5 Comparison and Discussion

The results presented above represent the state-of-the-art power levels for narrow-linewidth, near-diffraction limited hybrid MOPAs and All-solid PBGF MOPAs respectively. The previous record for each fiber type was demonstrated at the weak Yb emission spectral region near 1178 nm. Direct comparison studies at 1178 nm were not possible because the photonic lattice of each fiber was not designed for propagation at 1178 nm.

With the exception of the 35.5/355 μm core/clad hybrid fiber, all microstructured fibers studied were negatively impacted by MI. Ideally, a well-designed fiber waveguide suitable for power scaling would have MI and SBS thresholds within $\sim 10\%$ of one another. Neither of these fiber designs reached this criterion. The theoretical single-frequency SBS limit of the PBGF was much larger than the observed MI threshold when the estimated g_B from the pump probe experiment is used. The SBS limits of the hybrid fiber are also much larger than the observed MI limit when PRBS phase broadening is implemented because no Stokes light was observed during power scaling with the 1 GHz, 15 bit sequence utilized. Waveguide designs for these microstructured fibers, therefore, must concentrate on implementing more rigorous MI mitigation techniques.

In addition to optimizing the waveguide for MI suppression, experimental power scaling systems can improve MI resistance with proper design. For example, seeding a hexagonal waveguide core with a circular beam will engender unwanted coupling to higher-order core modes or cladding modes. This can be improved by designing phase screens that morph the collimated circular seed beam to a converging, hexagonal beam. Additionally, pre-amplifiers utilizing microstructured fiber can be designed so that the output of the pre-amplifier has similar transverse beam shape as the final-stage amplifier.

The hybrid fiber demonstrated Raman suppression as explained in chapter 1 with the experimental core transmission spectrum demonstrating high losses for wavelengths > 1110 nm because the PBG filter deterministically was designed to suppress the silica Raman peak at 1120 nm. The PBGF was not tested directly for spectral transmission/rejection at wavelengths > 1090 nm. Although each fiber was not able to reach power levels in which spontaneous Raman scattering becomes detrimental to laser linewidth, continuing to implement these suppression techniques will be necessary if/when microstructured fibers sufficiently suppress SBS and MI.

The glass composition of the active regions in each microstructured fiber was different with the PBGF composed of Yb-doped phosphate glass while the hybrid fiber contained Yb-doped pure silica with Al and F used to match the optical refractive index. Each glass composition has advantages and disadvantages. The phosphate-doped glass permits higher ytterbium concentration without photodarkening [11], but the ytterbium

gain spectrum is blue-shifted [29] which causes both absorption and emission at 1064 nm to be weakened compared to the non-phosphate equivalent for a constant doping concentration. In addition, phosphate fibers suffer from higher scattering cross-sections [30]. Non-phosphate glasses have lower intrinsic loss at 1 μm and benefit from a higher emission cross-section, but suffer from photodarkening when ytterbium doping concentrations are less than half of that found in phosphate-doped glass.

The weaker emission cross-section at 1064 nm of the phosphate glass would cause this glass composition to underperform compared to the non-phosphate equivalent in terms of reliable amplification limitations. It is understood that ASE becomes problematic in traditional pure-silica-doped ytterbium fiber amplifiers when amplification exceeds ~ 17 dB, although 22 dB amplification has been reported [31]. Amplification beyond 17 dB can lead to parasitic lasing at the ytterbium gain peak of ~ 1030 nm and/or pulsing. The ASE problem is exacerbated for step-index phosphate fibers because the emission cross-section is weaker at 1064 nm and the gain peak is near 1020 nm. The phosphate-based PBGF, however, has the potential to mitigate the ASE threshold of 17 dB amplification because spectral filtering can significantly reduce ASE levels in the core.

5. Conclusion

High-power ytterbium-doped fiber amplifiers designed with advanced waveguide concepts are characterized and power scaled. Fiber waveguides utilizing cladding microstructures to achieve wave guidance via the photonic bandgap (PBG) and a combination of PBG and modified total internal reflection (MTIR) have been proposed as viable single-mode waveguides. Such novel structures allow larger core diameters (>35 μm diameters) than conventional step-index fibers while still maintaining near-diffraction limited beam quality. These microstructured fibers are demonstrated as robust single-mode waveguides at low powers and are power scaled to realize the thermal power limits of the structure. Here above a certain power threshold, these coiled few-mode fibers have been shown to be limited by modal instability (MI); where energy is dynamically transferred between the fundamental mode and higher-order modes. Nonlinear effects such as stimulated Brillouin scattering (SBS) are also studied in these

fiber waveguides as part of this dissertation. Suppressing SBS is critical towards achieving narrow optical bandwidths (linewidths) necessary for efficient fiber amplifier beam combining. Towards that end, new effects that favorably reduce acoustic wave dispersion to increase the SBS threshold are discovered and reported.

The first advanced waveguide examined is a Yb-doped 50/400 μm diameter core/clad PBGF. The PBGF is power scaled with a single-frequency 1064 nm seed to an MI-limited 410 W with 79% optical-to-optical efficiency and near-diffraction limited beam quality ($M2 < 1.25$) before MI onset. To this author's knowledge, this represents $>2.4\times$ improvement in power output from a PBGF amplifier. During power scaling, a remarkably low Brillouin response was elicited from the fiber even when the ultra large diameter 50 μm core is accounted for in the SBS threshold equation. Subsequent interrogation of the Brillouin response in a pump probe Brillouin gain spectrum diagnostic estimated a Brillouin gain coefficient, g_B , of 0.62×10^{-11} m/W; which is $4\times$ reduced from standard silica-based fiber. A finite element numerical model that solves the inhomogeneous Helmholtz equation that governs the acoustic and optical coupling in SBS is utilized to verify experimental results with an estimated $g_B = 0.68 \times 10^{-11}$ m/W. Consequently, a novel SBS-suppression mechanism based on inclusion of sub-optical wavelength acoustic features in the core is proposed.

The second advanced waveguide analyzed is a 35/350 μm diameter core/clad fiber that achieved wave guidance via both PBG and MTIR, and is referred to as a hybrid fiber. The waveguide benefits mutually from the amenable properties of PBG and MTIR wave guidance because robust single-mode propagation with minimal confinement loss is assured due to MTIR effects, and the waveguide spectrally filters unwanted wavelengths via the PBG effect. The waveguide employs annular Yb-doped gain tailoring to reduce thermal effects and mitigate MI. Moreover, it is designed to suppress Raman processes for a 1064 nm signal by attenuating wavelengths > 1110 nm via the PBG effect. When seeded with a 1064 nm signal deterministically broadened to ~ 1 GHz, the hybrid fiber was power scaled to a MI-limited 820 W with 78% optical-to-optical efficiency and near diffraction limited beam quality of $M2 \sim 1.2$ before MI onset. This represents a $14\times$ improvement in power output from a hybrid fiber, and

demonstrates that this type of fiber amplifier is a quality candidate for further power scaling for beam combining.

6. References

1. R. G. Smith, "Optical Power Handling Capacity of Low Loss Optical Fibers as Determined by Stimulated Raman and Brillouin Scattering," *Applied Optics*, vol. 11, no. 11, pp. 2489-2494, 1972.
2. M. Hildebrandt, S. Busche, P. Webels, M. Frede and D. Kracht, "Brillouin Scattering Spectra in High-Power Single-Frequency Ytterbium Doped Fiber Amplifiers," *Optics Express*, vol. 16, no. 20, pp. 15970-15979, 2008.
3. N. A. Brilliant, "Stimulated Brillouin Scattering in a Dual-Clad Fiber Amplifier," *Journal of the Optical Society of America B*, vol. 19, no. 11, pp. 2551-2557, 2002.
4. C. Zeringue, C. Vergien and I. Dajani, "Pump-Limited, 203 W, Single-Frequency Monolithic Fiber Amplifier Based on Laser Gain Competition," *Optics Letters*, vol. 36, no. 5, pp. 618-620, 2011.
5. C. Zeringue, "A Theoretical and Experimental Analysis of SBS Suppression Through Modification of Amplifier Seed," PhD Dissertation, University of New Mexico, 2011.
6. N. Shibata, R. G. Waarts and R. P. Braun, "Brillouin-Gain Spectra for Single-Mode Fibers Having Pure-Silica, GeO₂-doped, and P₂O₅-Doped Cores," *Optics Letters*, vol. 12, no. 4, pp. 269-271, 1987.
7. M. Nikles, L. Thevenaz and P. A. Robert, "Brillouin Gain Spectrum Characterization in Single-Mode Optical Fibers," *Journal of Lightwave Technology*, vol. 15, no. 10, pp. 1842-1851, 1997.
8. G. Agrawal, *Nonlinear Fiber Optics*, Waltham, MA: Elsevier Academic Press, 2013.
9. T. Horiguchi, M. Tateda, N. Shibata and Y. Azuma, "Brillouin Gain Variations Due to a Polarization-State Change of the Pump or Stokes Fields in Standard Single-Mode Fibers," *Optics Letters*, vol. 14, no. 6, pp. 329-331, 1989.
10. M. Chen, A. Shirikawa, X. Fan, K.-i. Ueda, C. B. Olausson, J. K. Lyngso and J. Broeng, "Single Frequency Ytterbium Doped Photonic Bandgap Fiber Amplifier at 1178 nm," *Optics Express*, vol. 20, no. 19, pp. 21044-21052, 2012.

11. Y. W. Lee, S. Sinha, M. J. F. Digonnet, R. L. Byer and S. Jiang, "Measurement of High Photodarkening Resistance in Heavily Yb³⁺-Doped Phosphate Fibres," Electronics Letters, vol. 44, no. 1, pp. 14-16, 2008.
12. Y.-W. Lee, "Power Scaling of Yb-Doped Phosphate Fiber Laser and Amplifiers," PhD Dissertation, Stanford University, 2008.
13. B. Ward and J. Spring, "Finite Element Analysis of Brillouin Gain in SBS-Suppressing Optical Fibers with Non-Uniform Acoustic Velocity Profiles," Optics Express, vol. 17, no. 18, pp. 15685-15699, 2009.
14. K. Saitoh and M. Koshiba, "Full-Vectorial Imaginary-Distance Beam Propagation Method Based on a Finite Element Scheme: Application to Photonic Crystal Fibers," IEEE Journal of Quantum Electronics, vol. 38, no. 7, pp. 927-931, 2002.
15. M. Koshiba and Y. Tsuji, "Curvilinear Hybrid Edge/Nodal Elements with Triangular Shape for Guided-Wave Problems," Journal of Lightwave Technology, vol. 18, no. 5, pp. 737-743, 2000.
16. A. V. Smith and J. J. Smith, "Mode Instability in High Power Fiber Amplifiers," Optics Express, vol. 19, no. 11, pp. 10180-10192, 2012.
17. C. Jauregui, T. Eidam, J. Limpert and A. Tünnermann, "Impact of Modal Interference on the Beam Quality of High-Power Fiber Amplifiers," Optics Express, vol. 19, no. 4, pp. 3258-3271, 2011.
18. J. Limpert, N. Deguil-Robin, I. Manek-Hönniger, F. Salin, F. Röser, A. Liem, T. Schreiber, S. Nolte, H. Zellmer, A. Tünnermann, J. Broeng, A. Peterson and C. Jakobsen, "High Power Rod-type Photonic Crystal Fiber Laser," Optics Express, vol. 13, no. 4, pp. 1055-1058, 2005.
19. C. Jauregui, T. Eidam, H.-J. Otto, F. Stutzki, F. Jansen, J. Limpert and A. Tünnermann, "Physical Origin of Mode Instabilities in High Power Fiber Laser Systems," Optics Express, vol. 20, no. 12, pp. 12912-12925, 2012.
20. C. Jauregui, T. Eidam, H.-J. Otto, F. Stutzki, F. Jansen, J. Limpert and A. Tünnermann, "Physical Origin of Mode Instabilities in High Power Fiber Laser Systems," Optics Express, vol. 20, no. 12, pp. 12912-12925, 2012.

21. H.-J. Otto, N. Modsching, C. Jauregui, J. Limpert and A. Tünnermann, "Impact of Photodarkening on the Mode Instability Threshold," *Optics Express*, vol. 23, no. 12, pp. 15265-15277, 2015.
22. H. M. Pask, R. J. Carman, D. C. Hanna, A. C. Tropper, P. R. Mackechnie and J. M. Dawes, "Ytterbium-Doped Silica Fiber Lasers: Versatile Sources for the 1-1.2 micron Region," *IEEE Journal of Selected Topics in Quantum Electronics*, vol. 1, no. 1, pp. 2-13, 1995.
23. N. A. Naderi, I. Dajani and A. Flores, "High-Efficiency, Kilowatt 1034 nm All-Fiber Amplifier Operating at 11 pm Linewidth," *Optics Letters*, vol. 41, no. 5, p. 1018, 2016.
24. S. Naderi, I. Dajani, J. Grosek and T. Madden, "Theoretical and Numerical Treatment of Modal Instability in High-Power Core and Cladding Pumped Raman Fiber Amplifiers," *Optics Express*, vol. 24, no. 15, p. 16550, 2016.
25. B. Anderson, A. Flores, R. Holten and I. Dajani, "Comparison of Phase Modulated Schemes for Coherently Combined Fiber Amplifiers," *Optics Express*, vol. 23, no. 21, pp. 27046-27060, 2015.
26. C. Zeringue, I. Dajani, S. Naderi, G. T. Moore and C. Robin, "A Theoretical Study of Transient Stimulated Brillouin Scattering in Optical Fibers Seeded with Phase-Modulated Light," *Optics Express*, vol. 20, no. 19, pp. 21196-21213, 2012.
27. B. Pulford, T. Ehrenreich, R. Holten, F. Kong, T. W. Hawkins, L. Dong and I. Dajani, "400-W Near Diffraction-Limited Single-Frequency All-Solid Photonic Bandgap Fiber Amplifier," *Optics Letters*, vol. 40, no. 10, pp. 2297-2300, 2015.
28. R. Koch, W. A. Clarkson, D. C. Hanna, S. Jiang, M. J. Myers, D. Rhonehouse, S. J. Hamlin, U. Griebner and H. Schonngel, "Efficient Room Temperature CW Yb:Glass Laser Pumped by a 946 nm Nd:YAG Laser," *Optics Communications*, vol. 134, no. 1-6, pp. 175-178, 1997.
29. Y. Jeong, J. Nilsson, J. K. Sahu, D. N. Payne, R. Horley, L. M. B. Hickey and P. W. Turner, "Power Scaling of Single-Frequency Ytterbium-Doped Fiber Master-Oscillator Power-Amplifier Sources up to 500 W," *IEEE Journal of Selected Topics in Quantum Electronics*, vol. 13, no. 3, pp. 546-551, 2007.

30. Y.-W. Lee, M. J. F. Digonnet, S. Sinha, K. E. Urbanek, R. L. Byer and S. Jiang, "High Power Yb³⁺-Doped Phosphate Fiber Amplifier," IEEE Journal of Selected Topics in Quantum Electronics, vol. 15, no. 1, pp. 93-102, 2009.
31. M. D. Mermelstein, "SBS Threshold Measurements and Acoustic Beam Propagation Modeling in Guiding and Anti-Guiding Single-Mode Optical Fibers," Optics Express, vol. 17, no. 18, pp. 16225-16237, 2009.

List of Acronyms

ACDC	Alternating Current Direct Current
AFRL	Air Force Research Laboratory
ASE	Amplified Spontaneous Emission
BG	Band Gap
BGS	Brillouin Gain Spectrum
BPM	Beam Propagation Model
BS	Beam Splitter
CAD	Computer Aided Design
CPRFA	Cladding-Pumped Raman Fiber Amplifiers
DS	Dual-source
FWHM	Full Width at Half Maximum
IPG	(Company Name)
LMA	Large Mode Area
MI	Modal Instability
MO	Master Oscillator
MOPA	Master Oscillator Power Amplifier
MOPA	Master Oscillator Power Amplifier
MTIR	Modified Total Internal Reflection
NKT	(Company Name)
NPRO	Non-planar Ring Oscillator
OFS	(Company Name)
OSA	Optical Spectrum Analyzers
PBGF	Photonic Band Gap Fiber
PBS	Polarization Beam Splitter
PCF	Photonic Crystal Fiber
PER	Polarization Extinction Ratio

PM	Power Meters
RE	Rare-Earth
RF	Radio Frequency
RFA	Raman Fiber Amplifiers
RFSA	Radio Frequency Spectrum Analyzer
SBS	Stimulated Brillouin Backscattering
SFPI	Scanning Fabry Perot Interferometer
SNR	Signal-to-Noise Ratio
SRS	Stimulated Raman Scattering
TIR	Total Internal Reflection
Yb	Ytterbium
YDFA	Ytterbium Doped Fiber Amplifier

DISTRIBUTION LIST

DTIC/OCP

8725 John J. Kingman Rd, Suite 0944
Ft Belvoir, VA 22060-6218

1 cy

AFRL/RVIL

Kirtland AFB, NM 87117-5776

1 cy

Benjamin Pulford

Official Record Copy

AFRL/RDLT

1 cy